THE ASTROPHYSICAL JOURNAL, 334:815–840, 1988 November 15

AN ALL-SKY SEARCH FOR MOLECULAR CIRRUS CLOUDS

F. X. DÉSERT
Laboratory of Astronomy and Solar Physics, Goddard Space Flight Center

D. BAZELL
Applied Research Corporation

AND

F. BOULANGER
Infrared Processing and Analysis Center, California Institute of Technology
Received 1987 September 28; accepted 1988 May 17

ABSTRACT

The infrared (IR) brightness of the sky, once the zodiacal light is removed, has been shown to be highly correlated with the total gaseous (H I and H_2) content of the interstellar medium. We have used this correlation to deduce a map of infrared-excess gas by subtracting, in an appropriate way, the H I component from the infrared brightness. Having computed the correlation between the 100 μm IR and 21 cm H I emission data (with pixels of 20′) for each small solid angle in the sky (~ 10 deg^2), we deduced the residual for each pixel. The large IR-excess residuals that are spatially connected define IR-excess clouds (IRECs). The method is limited to part of the sky where the heating of the dust is relatively uniform and allows the identification of the nearby molecular clouds at high Galactic latitude ($|b| \gtrsim 5°$) and/or the clouds which have local heating sources or a larger dust-to-gas ratio than the average.

An all-sky map and a catalog of 516 significant clouds are presented and statistically analyzed. About half the CO clouds at $|b| \gtrsim 25°$ observed by Magnani, Blitz, and Mundy coincide with entries in our catalog of IRECs, and are used as a comparison sample to assess the validity and the limits of our method. Further observations, particularly in CO, could help in understanding the nature of the objects in the present catalog.

Spatial variations of the IR-to-gas ratio and locations of IR-deficient clouds also constitute results of the performed analysis.

Subject headings: interstellar: molecules — nebulae: general

I. INTRODUCTION

Nearby high-latitude clouds can provide important information about the physics of interstellar matter in the Galaxy because they can be observed with higher spatial resolution and less confusion than clouds in the Galactic plane. Although the principal constituent of the local ISM, atomic hydrogen, has been well-studied through the 21 cm line, it is only recently that the local molecular component of the ISM has been observed, aside from the largest concentrations: Taurus, Orion, and Ophiuchus regions (see, e.g., Dame *et al.* 1987). Taking a sample of regions (~ 400) at high Galactic latitudes where they found evidence of visual extinction, Magnani, Blitz, and Mundy (1985, hereafter MBM; see also Blitz, Magnani, and Mundy 1984) detected the presence of CO molecules in about one-fifth of their sample directions. These high-latitude molecular clouds of a few to tens of solar masses have been shown to be very local, within ~ 100 pc of the Sun (MBM; Magnani and de Vries 1986). Another smaller molecular survey, this time in the southern hemisphere, was done by Keto and Myers (1986, hereafter KM). An estimate of the completeness of these surveys is discussed, after additional observations, by Magnani, Lada, and Blitz (1986).

Interstellar clouds can be traced via their dust content, which is observed either in extinction (see MBM and KM) or through thermal emission. The latter approach has become especially valuable since the release of the enormous volume of data from the *IRAS* (Beichman *et al.* 1985; hereafter *IRAS Explanatory Supplement*). Both the high-latitude clouds studied by Low *et al.* (1984) and Boulanger, Baud, and van Albada (1985) made essentially of atomic hydrogen gas and some of the high-latitude molecular clouds in the MBM sample have been shown to possess their counterparts in the *IRAS* maps (Weiland *et al.* 1986; de Vries, Heithausen, and Thaddeus 1987, hereafter VHT).

The main purpose of the present paper is to present a systematic survey of the high-latitude IR-excess clouds obtained by using the almost complete maps of the sky in the IR and H I 21 cm line (at normal velocities). Outside of giant molecular clouds and H II regions the correlation between the IR–100 μm and H I maps has been shown to be quite good, initially by Low *et al.* (1984) and more quantitatively by Boulanger, Baud, and van Albada (1985) and Boulanger and Pérault (1988, hereafter BP). At high Galactic latitudes, BP have found that most of the IR emission is from dust associated with atomic hydrogen. However, the dispersion around the IR–H I correlation is larger than the uncertainties in the observations. Structures in the excess IR map could reveal high Galactic latitude clouds which differ from clouds with normal cirrus properties. The basic assumption is that the *IRAS* data measure the integrated emission of dust along the line of sight associated with the total hydrogen column density, whereas the H I data measure only the column density of atomic hydrogen within normal velocities. Thus, excess emission at 100 μm may be due to several causes: (1) dust associated with H I at high velocities; (2) dust associated with diffuse molecular clouds (H_2 clouds) as mentioned above; (3) dust associated with peculiar H I clouds

which have either an unusual dust-to-gas ratio or heating sources different from the interstellar radiation field (ISRF); (4) dust associated with ionized gas; (5) solar system objects; (6) extragalactic objects. Solar system objects (beside Saturn) are unlikely to contribute much in the 100 μm *IRAS* map, hence, in the IR-excess map.

Such a method finds a confirmation and a justification, besides the ones given above, in the maps shown by VHT of the H I, IR, and CO data of the molecular cirrus around $l_{II} = 145°$ and $b_{II} = 38°$. Other goals of the present paper are to briefly discuss the spatial variations of the IR-to-gas ratio (see § IV*a*) and the IR-deficient clouds (see § V*f*) that can also be found by the above method.

After describing the IR and H I surveys (§ II), we present in § III the correlation analysis method used for subtracting contribution of atomic gas to the IR data. In § IV, the IR-excess map of the sky is shown and we derive a catalog of the most significant clouds (Table 1). Some associations with previously known objects and some discussions of the preceding results are made in § V.

II. THE TWO SURVEYS OF THE SKY AT 0.01 AND 21 CENTIMETRES

a) The IRAS Survey of the Sky

The *Infrared Astronomical Satellite* (*IRAS*) has provided an almost complete survey of the sky in four broad wavelength bands centered at 12, 25, 60, and 100 μm. The data consist of point sources as well as a diffuse background emission due to the emission of the interplanetary and interstellar dust. Using the time-ordered Zodiacal History File (*IRAS Explanatory Supplement*), the interstellar dust emission and the zodiacal dust emission have been separated (see BP), leaving a residual zodiacal emission of $\sim 1\%$ of its initial value. In order to trace the *cold* dust mass in a given direction, we have used the 100 μm observations map because it has the best signal-to-noise ratio. The generated map has a resolution of $1/2° \times 1/2°$ and has been sampled each 1/3° (1 pixel equals 3.38×10^{-5} sr) in order to be compared with the H I surveys. The zero level of the 100 μm map is set in a way that the emission at 100 μm would vanish for a vanishing H I column density (see BP). Throughout this work, we have used an area-conserving projection, centered at the Galactic anticenter, from the Galactic coordinates l_{II} and b_{II} to the projected coordinates L and b_{II}, where

$$L = 180° + (l_{II} - 180°) \cos b_{II} , \qquad (2.1)$$

so that meridians become arcs of sinusoids and parallels (constant latitude lines) becomes horizontal lines. The noise in the *IRAS* measurements is of the order 0.1 MJy sr^{-1}, but because of striping phenomena and zodiacal light subtraction, the actual (non-Gaussian) noise is more like 0.5 MJy sr^{-1}. However, the method described in § III*b* allows us to improve this value, because we can get rid of a large part of the striping noise and the large-scale uncertainties in the zodiacal light subtraction through the IR–H I correlation.

A brightness of 0.1 MJy sr^{-1} in one pixel corresponds to a flux of ~ 3.4 Jy. External galaxies and other point sources can contaminate the IR maps at that level. However, as can be deduced from the *IRAS* point-source catalog, only one galaxy above 3.4 Jy is expected for every 60 pixels. We return to this question in § V*b*.

b) The H I Surveys

In order to cover as much sky as possible, two H I surveys have been combined. The northern survey ($\delta \geq -30°$) was conducted by Heiles and Habing (1974) for $|b| \geq 10°$, with a H I velocity integration range of -92 to 75 km s^{-1} and Weaver and Williams (1973) for $|b| \leq 10°$ (width of velocity coverage: 250 km s^{-1}). The southern survey ($\delta \leq -30°$) is built from the observations by Colomb, Pöppel, and Heiles (1980) for $|b| \geq 10°$ and Henderson, Jackson, and Kerr (1982) for $|b| \leq 10°$ ($|v| < 38$ km s^{-1}, the Galactic center (10° wide) is not covered). An antenna efficiency of 1/1.15 has been taken into account for the northern survey, and the overlapping region of the two surveys ($-30° \leq \delta \leq -25°$) was used to scale the southern survey (see Colomb *et al.* 1980). We assumed that the 21 cm emission is optically thin, and the integrated brightness temperature was converted to an atomic hydrogen column density with the scaling factor 1.82×10^{18} H cm^{-2}/(K km s^{-1}) (e.g. Kerr 1968). The H I data have an initial sampling of $\Delta L \times \Delta b = 18' \times 36'$ (half beam size) in the northern hemisphere and $\Delta\delta = 1°$ (twice the beamwidth) in the southern hemisphere. They were then projected and sampled into a 1/3° grid following the projection formula (2.1). The effective resolution of this map is $\sim 2/3°$. The sky coverage is almost complete except for the region within 10° of the Galactic center, which would be excluded in any case by the method we discuss in § III.

There are two major problems in the H I map, which produce stripes that are on average of the order of 40 K km s^{-1} (70×10^{18} H cm^{-2}): (1) the stripes between different constant latitude lines (either galactic for the northern survey or equatorial for the southern survey) due to difficult spectral baseline removals; (2) the stray-radiation which corresponds to an extra signal coming from the Galactic plane through the far side lobes of the radiotelescope when it is pointing at high Galactic latitudes (see e.g. Lockman, Jahoda, and McCammon 1986). It is assumed here that the stray-radiation has little structure on scales less than $\sim 10°$ (see a similar assumption by Heiles, Stark, and Kulkarni 1981). In § III, we show how these problems appear in the data, and we propose a method to correct them, at least in a first-order approximation, by using the IR–H I correlation.

The uncertainty in the H I map is estimated to be of the order of 20–30 K km s^{-1} ($36–55 \times 10^{18}$ H cm^{-2}) in the northern survey and slightly more in the southern one (see Colomb *et al.* 1980).

III. THE CORRELATION ANALYSIS METHOD

a) The General Method

We make use of the linear correlation between the IR emission and the total hydrogen column density along a given line of sight, in order to deduce the infrared residual along each line of sight. The correlation is performed locally to eliminate any global variations of the correlation and also to remove stripes in the initial data.

Our basic procedure is summarized in the Appendix and detailed in the following. First, because both the H I and the IR data averaged over longitude at constant Galactic latitude follow a cosecant law, a global correlation is expected between the H I column density N_{HI} and the 100 μm brightness B_4 that could hide the local correlation we are computing. Therefore, we first removed the global cosecant laws (BP) from the initial

maps:

$$\langle N_{\rm H\,I}\rangle = 3.0 \times 10^{20}\ {\rm H\ cm^{-2}/sin}\,|b| \quad \text{for} \quad b \neq 0\,, \quad (3.1)$$

and

$$\langle B_4\rangle = 2.6\ {\rm MJy\ sr^{-1}/sin}\,|b| \quad (3.2)$$

(for $b = 0$, the values at $b = 1/3°$ of eqns. (3.1) and (3.2) are taken). BP have shown that the IR and H I residuals from the cosecant laws correlate, a proof that the IR is emitted mostly by the H I medium. We perform a linear least-squares fit to the correlation between $N_{\rm H\,I}$ and B_4, where both variables have the respective cosecant law removed. Strong point sources are not included by eliminating pixels with a relative 100 μm brightness of more than 8 MJy sr^{-1}. We then compute the excess of the IR emission over what is expected for a given H I column density, in each line of sight. In order to allow for possible slow variations of the slope S_{4h} and the intercept I_{4h}, the correlation analysis is performed locally (see below). This method introduces a bias in the sense that it underestimates the flux coming from very extended IR excess regions, but it allows us to get rid of stripes in the data (see § III*b*). Thus, we perform the fit separately for each small cell C on the sky with a size of $\Delta L = 20°$ by $\Delta b = 8°$. The value of the excess IR emission B_4^e is then deduced for each pixel i inside a smaller cell C' of dimensions $\Delta L' = 6°$ by $\Delta b' = 4°$ centered on the center of the cell C:

$$B_4^e(i) = B_4(i) - [N_{\rm H\,I}(i) - I_{4h}]/S_{4h}\,. \quad (3.3)$$

One can deduce the corresponding equivalent excess hydrogen column density $N_{\rm H}^e$ of the pixel i, assuming that the properties of the dust associated with the IR-excess gas are similar to those in the H I medium surrounding it:

$$N_{\rm H}^e(i) = B_4(i)S_{4h} - N_{\rm H\,I}(i) + I_{4h}\,. \quad (3.4)$$

The last assumption, similar to one made by VHT, is discussed in §§ IV and V. The procedure is then performed until the cells C' cover the entire sky, with the values of S_{4h} and I_{4h} in adjacent cells C' being calculated from overlapping cells C.

The size of the cell C (made of 1440 $\frac{1}{9}$ deg^2 pixels: 13° × 13°) is chosen in order that the statistics are large enough not to introduce significant errors and are bigger than the average size of the clouds that are we looking for. The cell C also is small enough to allow some possible variation of the H I–to–IR ratio on length scales larger than few tens of parsecs at a solar distance of 100 pc. The size of the cell C' is small enough (15% of C) so that the pixels inside do not strongly influence the correlation analysis. In the least-square fitting procedure, we assume that the IR data have a negligible uncertainty compared with the H I uncertainty, so that the B_4 variable is taken as the independent variable. Indeed, for an estimated average ratio of

$$S_{4h} \approx 1.2 \times 10^{20}\ {\rm H\ cm^{-2}/MJy\ sr^{-1}}\,, \quad (3.5)$$

deduced from the cosecant law (BP), an uncertainty of at least 36×10^{18} H cm^{-2} (20 K km s^{-1}) in the integrated H I column density corresponds to 0.3 MJy sr^{-1} which is at least 3 times the noise in the IR map. However, our choice of B_4 as the independent variable seems to lead to an underestimate of the slope S_{4h} as discussed in § IV*a*.

The analysis is complicated by the fact that the noise in the data is not the only source of scatter around the line of correlation. The resulting map of $N_{\rm H}^e$ (not shown here) shows some stripes at constant Galactic latitudes for the northern hemisphere and at constant declination for the southern hemisphere ($\delta \leq -30°$). These stripes must come from the H I data, because the radio telescopes surveyed the sky by scanning along these directions. Less pronounced are stripes which run along the *IRAS* scans (at constant solar elongations) and are probably due to residues of zodiacal emission or calibration uncertainties during the *IRAS* flight. We attempt a correction for these defects in the following section.

b) Destriping

In order to remove the stripes in the previous map, we use the fact that the IR and H I stripes are generally not in the same directions. We assume that they come mainly from a background unrelated to the correlated part of the H I and IR maps. Thus, we may assume that the stripes at constant latitude b in the northern hemisphere can be modeled as an H I–related background $G_h(b)$, independent of the longitude L, at least in each cell C (see § III*a*), and independent of $N_{\rm H\,I}$ (see, e.g., Heiles, Stark, and Kulkarni 1981). A good estimate of this background is therefore given by averaging the residuals (3.4) over lines of constant latitude (within 1/3°), inside each cell C:

$$G_h(b) \approx \langle N_{\rm H\,I}(i) - [B_4(i)S_{4h} + I_{4h}]\rangle_b = -\langle N_{\rm H}^e(i)\rangle_b\,, \quad (3.6)$$

where points farther than $\pm 5\ \sigma$ from the fitted line are discarded (σ is the rms dispersion of all the points around the fitted line). Another linear correlation is performed between B_4 and the corrected $N_{\rm H\,I}$–$G_h(b)$ to obtain the corrected residual for each pixel:

$$N_{\rm H}^{e\prime}(i) = B_4(i)S'_{4h} + I'_{4h} - \{N_{\rm H\,I}(i) - G_h[b(i)]\}\,. \quad (3.7)$$

This method can work only if the fraction of the cell covered with IR–excess clouds is small.

The same technique is applied in the southern sky ($\delta \leq -30°$), but with a constant declination averaging. In the cells overlapping the border of the two H I surveys, we successively applied both techniques.

The *IRAS* scans were made along constant elongations θ (*IRAS Explanatory Supplement*), i.e. constant angles between the line of sight and the direction of the Sun. We recall that a value of $\theta = 90°$ corresponds to a constant ecliptic longitude (λ). The 100 μm map was generated with HCON 1 and HCON 2 scans within 5° of the elongation of 90°. In order to remove *IRAS* stripes, rather than averaging the residues at constant elongation, which would have forced us to go back to the Zodiacal History File information, we averaged them at constant ecliptic longitude, which can be calculated for each pixel in the IR map described in § II*a*. The error in taking λ rather than θ is indeed not large because the variation of the ecliptic longitude λ with the ecliptic latitude β along a scan is given by

$$d\lambda/d\beta = \tan\beta\,\cos\theta(\cos^2\beta - \cos^2\theta)^{-1/2}\,. \quad (3.8)$$

Thus, for example, for an elongation of $\theta = 87.^\circ5$ (respectively 85°), the so-called "banana effect" (*IRAS Explanatory Supplement*) introduces a shift in λ of at most $1.^\circ3$ (respectively $2.^\circ7$) in an entire cell C if $\beta \leq 45°$. At higher latitudes the zodiacal emission is a less severe problem.

In summary, in order to remove the stripes in the maps, we have iterated the correlation analysis after having successively subtracted the H I and IR stripes (formulae [3.6], [3.7]). After each iteration, the points which are clearly anomalous (here we set the limit at 5 standard deviations, as deduced from inspection of few examples; see e.g. § III*c*) are rejected from the computation of the slope S_{4h} and the intercept I_{4h} of the next

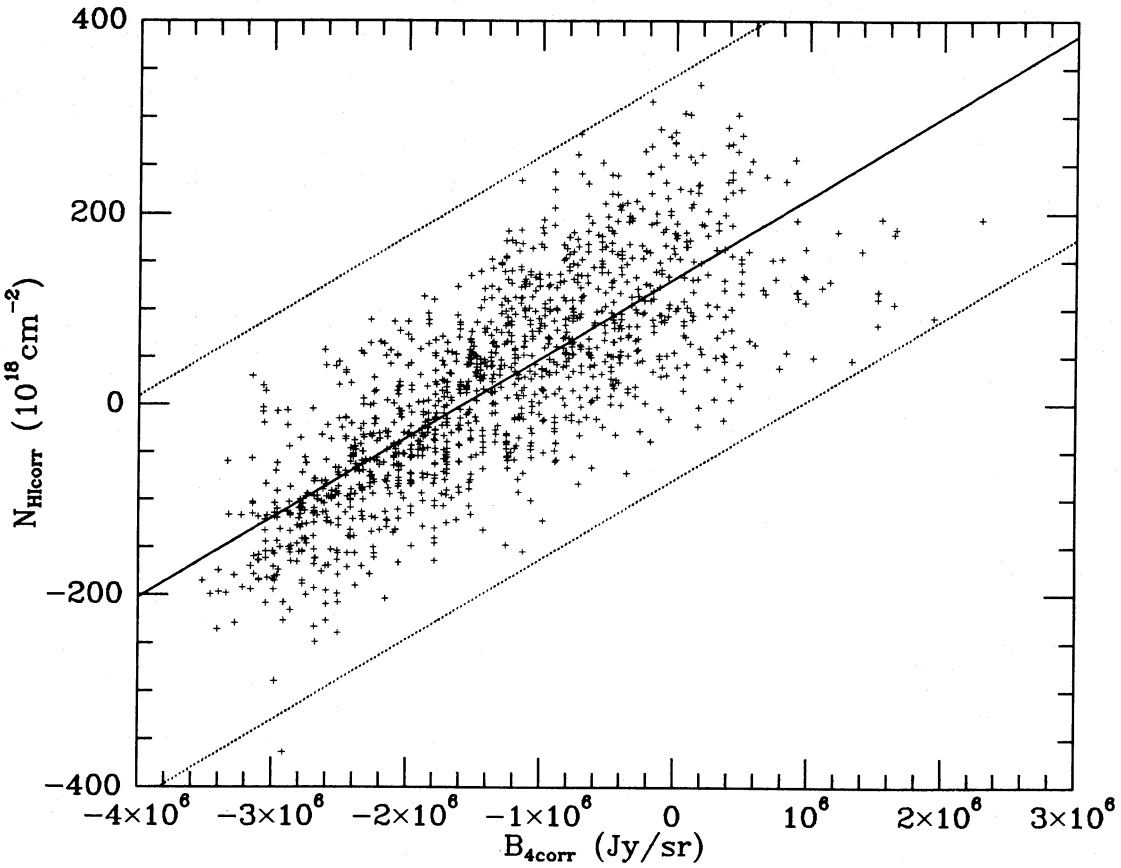

FIG. 1a

FIG. 1.—(*a*) Correlation diagram between the 100 μm brightness and H I column density (both having been corrected from the cosecant law expectation) in a small cell C in the sky (here centered at $L \approx 75°$ and $b \approx -25°$). Solid line shows the least-square fit to the points (each point represents 1/3° pixel). Dotted lines show the $\pm 3\,\sigma$ dispersion of the points around the fitted line. (*b*) The H I residue at each pixel from the fitted line in (*a*) are shown as a function of the galactic latitude. Solid line is the average of the residues at constant latitude. The large fluctuations of this line around zero show the stripiness of the H I data in the northern hemisphere. (*c*) The new correlation diagram is obtained when the solid line in (*b*) is subtracted from the H I data. The new least-squares fit takes into account only data which have a dispersion less than 5 σ in (*a*). (*d*) The IR residue of each pixel from the fitted line of (*c*) is plotted against the pixel ecliptic longitude. Solid line is the average of the residues at constant ecliptic longitude. (*e*) The final correlation diagram is obtained when the IR brightness has been corrected from the continuous line of (*d*).

iteration. The different steps of the method are summarized in the Appendix.

c) *An Example*

Figures 1*a*–1*e* shows a typical example of the method described in § III*b*. The cell C is here centered at $l_{II} = 64°$, $b_{II} = -25°$. The first iteration of the correlation analysis in Figure 1*a* helps in finding anomalous points (points falling more than 5 σ away from the fitted line, where σ is the rms deviations of the points around the fitted line). Using formula (3.6) (in the southern hemisphere, δ would replace b_{II}), we then calculate the H I background for use in destriping. These stripes at constant Galactic latitudes (the cell is in the northern hemisphere) are clearly in evidence in Figure 1*b*, where the amplitude of variation of the averaged residues can amount up to $\pm 50 \times 10^{18}$ H cm^{-2}. After having removed these H I stripes and discarded the more than 5 σ points, a subsequent correlation analysis is computed, as shown in Figure 1*c*. The fitted line has not varied very much, but the dispersion has been reduced. The stripes in the IR data are shown in Figure 1*d*, where the residues (in IR units) are plotted along with their average as a function of the ecliptic longitude. Figure 1*e* shows the final correlation adopted for the computation of the residues in the smaller cell C'. One can distinguish between the points which have an IR deficit or excess (respectively above or below the line) relative to the expectation value provided by the H I column density.

IV. THE RESULTS

a) *The Resulting Maps*

Figure 2 shows the location of weak or absent correlations between the hydrogen and IR maps (at the first iteration of the method). The correlation is present almost everywhere, beside a few isolated cells and the region close to the Galactic center. In the Galactic plane, the correlation exists but is certainly biased by the important molecular and H II components of the interstellar medium (Pérault *et al.* 1988, Sodroski *et al.* 1987).

Figure 3 shows the map of the gas-to-IR ratio $S_{4h} = dN_{HI}/dB_4$ (in units of H cm^{-2} per MJy sr^{-1}) found by the method described in the § III, after the last iteration. Dark areas correspond to regions where the IR flux is deficient relative to the mean value of the cosecant law in formula (3.5). The paradoxically high value of the slope in the Galactic plane (i.e.

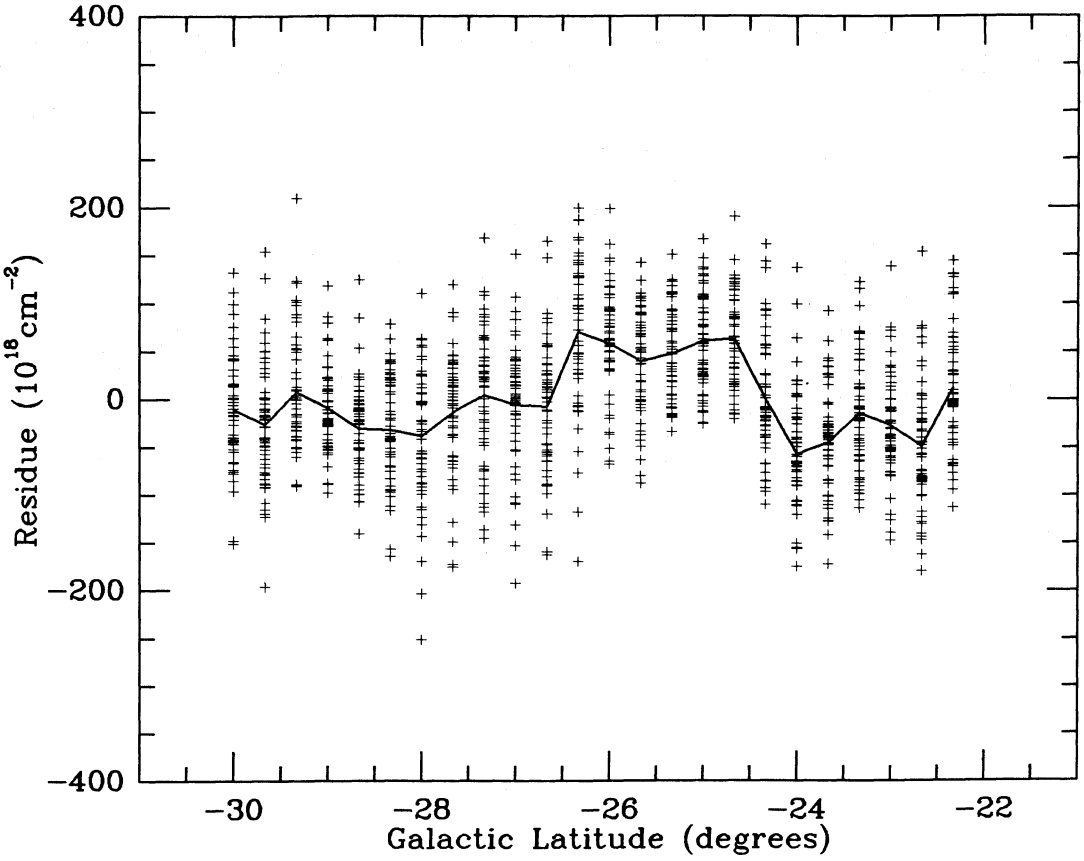

FIG. 1*b*

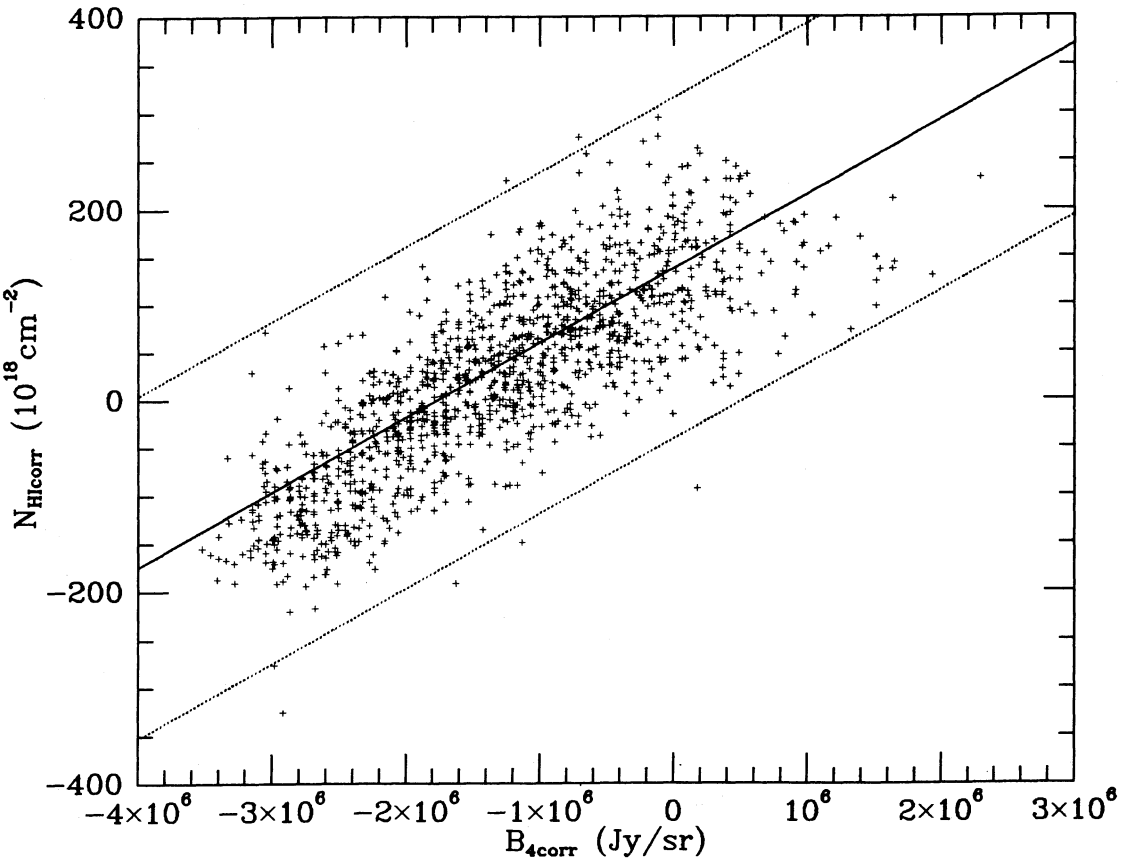

FIG. 1*c*

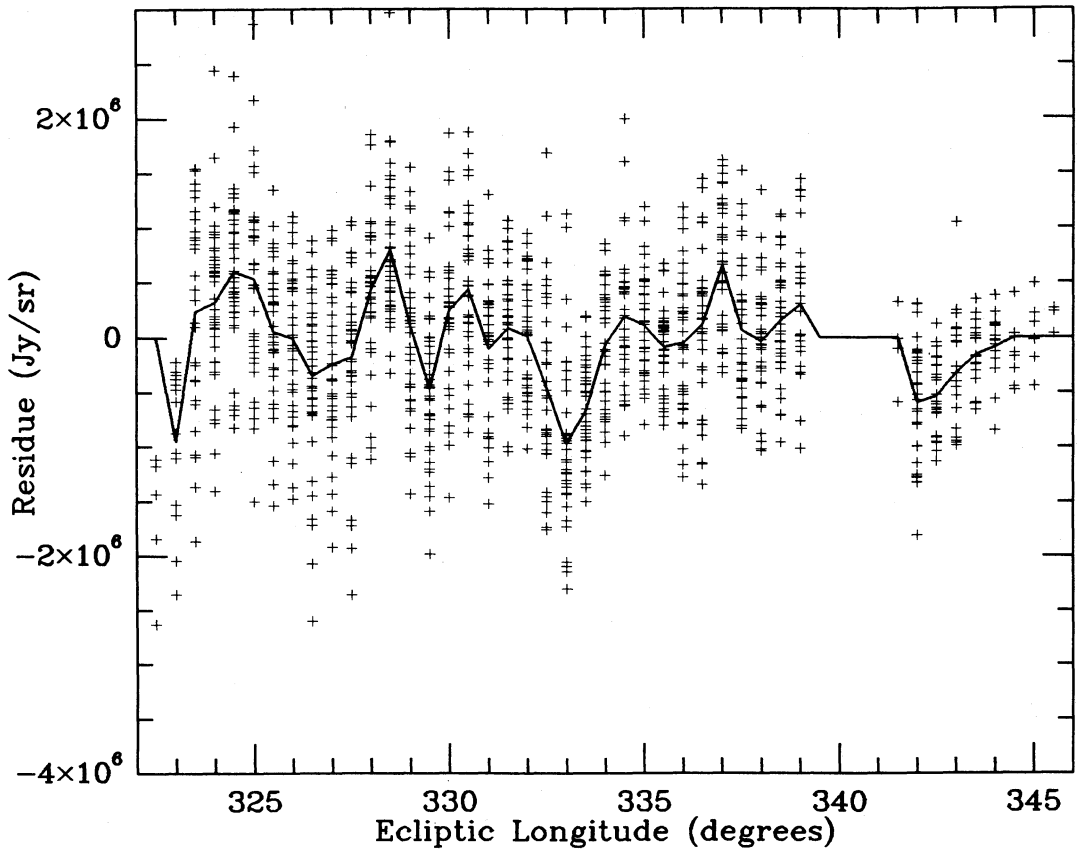

FIG. 1*d*

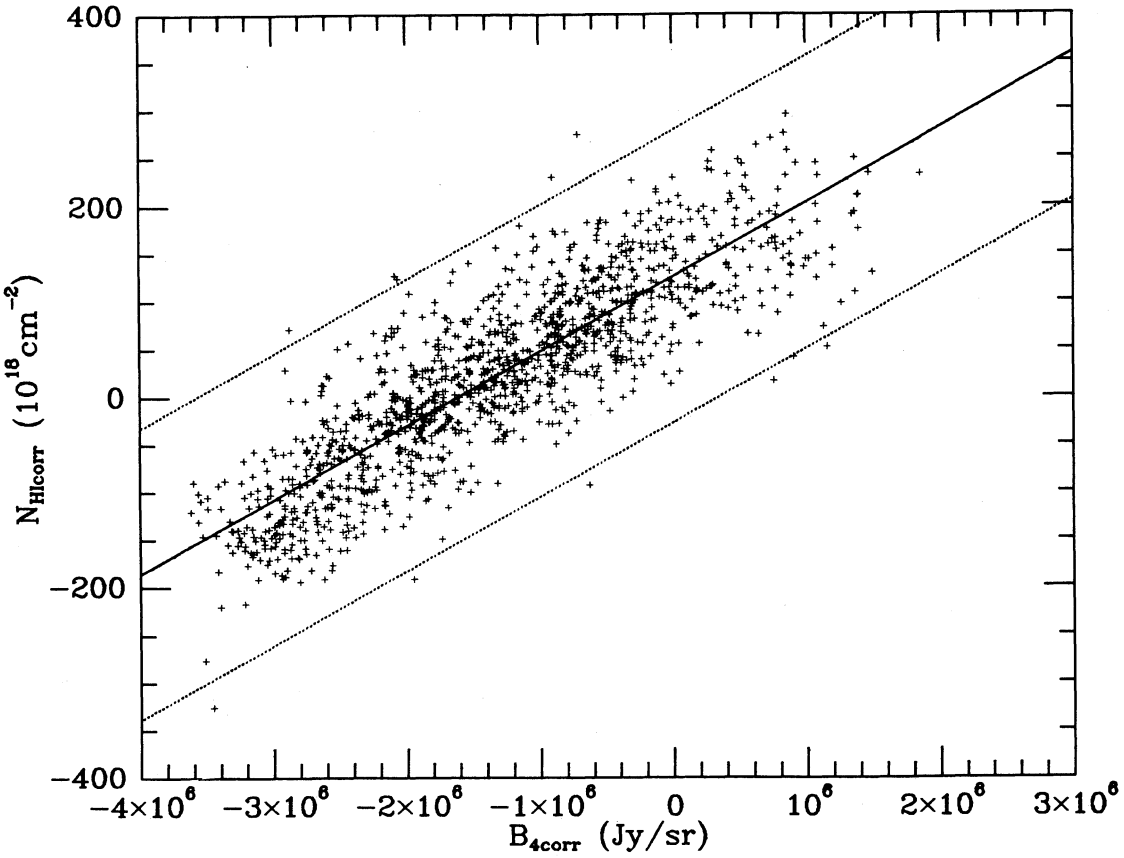

FIG. 1*e*

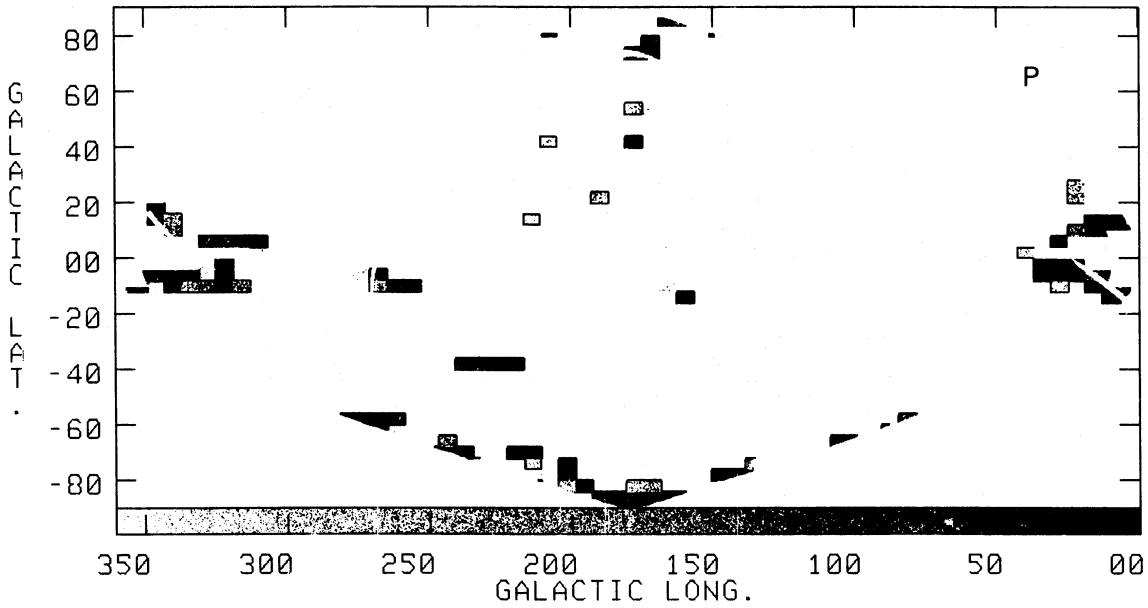

FIG. 2.—Map showing the goodness of fit in each cell C, as measured by the probability P that a correlation coefficient can be randomly generated that is larger than the one observed. It is given by $P \approx [(N-2)/2/\pi]^{1/2}(1-r^2)^{(N-2)/2}$, where N is the number of points and r is the correlation coefficient. Contour level is at $P = 5\%$. White areas correspond to $P \leq 0.3\%$. The map (like all the following ones) is in the area-conserving coordinates L (see formula [2.1]) and b_{II}, and is centered at the Galactic anticenter. L is equal to l_{II} only in the Galactic plane.

low IR) can be explained at least near the anticenter by the fact that a large column density of hydrogen gas outside the solar circle is present at these low latitudes. This gas is likely to contain less dust and/or its dust is heated by a reduced interstellar radiation field (ISRF) (Pérault *et al.* 1988).

The results of the correlation analysis are doubtful because the IR emissivity per H atom varies along the line sight. Figure 3 shows that local variations of the gas–to–IR ratio can amount up to a factor of 4. Burstein and Heiles (1978) previously claimed to see spatial variations of the gas-to-reddening ratio of up to a factor 4, where the reddening is measured by galaxy counts. However, we observed longitude variations of S_{4h} averaged over $20 < |b| < 64°$, as in Burstein and Heiles (1978), of only $\pm 20\%$, which are, moreover, uncorrelated with their Figure 4*b*. Therefore, it is not clear how local variations of S_{4h} can be interpreted: either due to gas-to-dust

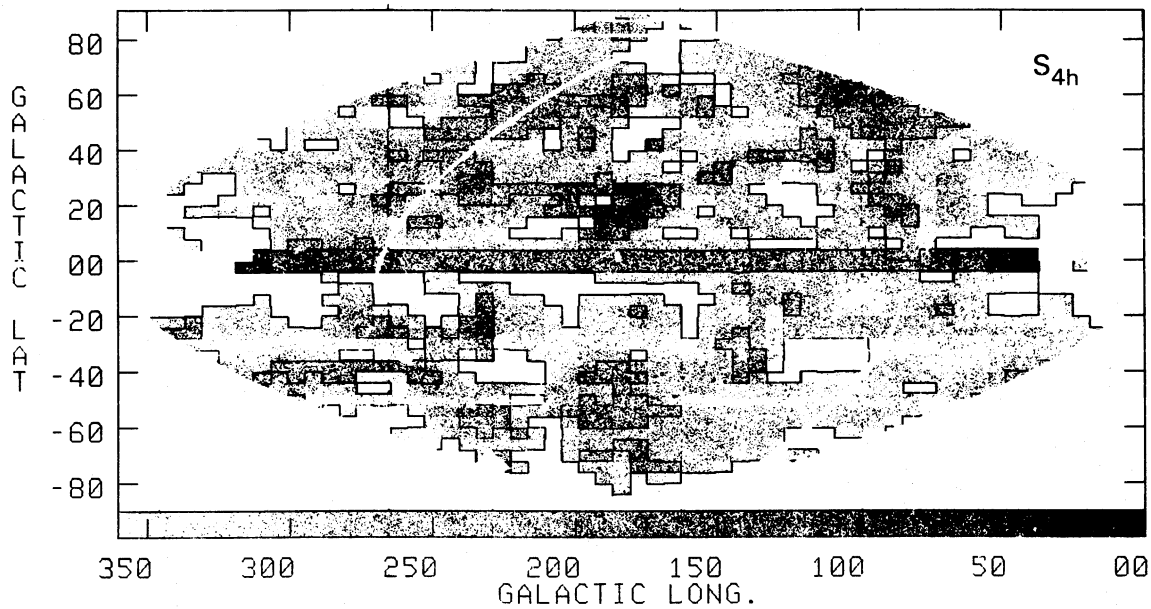

FIG. 3.—Map of the H I–to–IR brightness ratio S_{4h}, deduced from the correlation analysis developed in § III. The smallest rectangles in the map give the size of the cell C'. The gray-scale range is from 0.5 to 2 10^{20} H cm^{-2}/MJy sr^{-1}, and the contour levels are 0.5, 1, and 2 × 10^{20} H cm^{-2}/MJy sr^{-1}. White areas correspond to relatively high infrared emission regions of the sky.

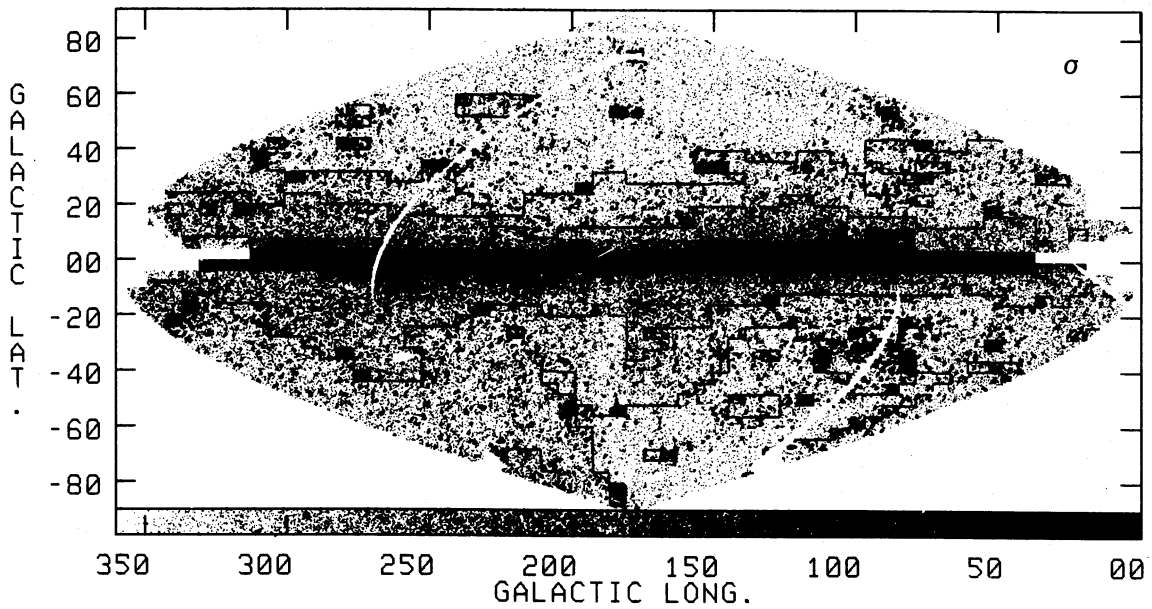

FIG. 4.—Map of the rms dispersion σ of the residues N_H^e around zero. The gray-scale ranges from 0 to 5 × 10^{20} H cm^{-2}. Contour levels are 0.5 and 1 × 10^{20} H cm^{-2}. Note that the dispersion is larger (i.e. darker in the figure) in the southern hemisphere (lower left part of the map), in the Orion-Taurus complex (south of the Galactic anticenter) and in the Galactic plane where the infrared emission is not only due to the H I medium. White areas correspond to blanked pixels due to a lack of either H I or *IRAS* data.

or ISRF variations. Furthermore, the average of S_{4h} at constant latitude reveals no systematic variations by more than ±10% for $|b| > 20°$ (it decreases for lower latitudes owing to heating sources, especially for $-20° \leq b \leq 0°$). The average value of S_{4h} (0.77 × 10^{20} H cm^{-2} MJy^{-1} sr) is lower than the cosecant law value (formula [3.5]) deduced by BP. That we used the IR brightness as the independent variable may explain the discrepancy. Indeed, we have repeated the method of § III, using the H I column density as the independent variable, and found that the slope is now 1.9 × 10^{20} H cm^{-2} MJy^{-1} sr), i.e. larger than the cosecant law (3.5). In summary, the gas-to-IR ratio varies on an angular scale of few tens of degrees, but there are no obvious systematic global variations of this ratio with either the latitude or the longitude.

The difference in the quality of the data between the northern and southern hemispheres is clearly shown by displaying in Figure 4 the map of the rms (hereafter σ) of the residuals obtained after the last correlation analysis in the iteration procedure described in § III*b* and in the Appendix. Actually, the value of σ is an upper estimate of the true noise in the initial data, because real but low IR excesses contribute to increase σ. The southern hemisphere along with the Galactic plane and a few isolated spots are clearly noisier than the remainder of the map. For the Galactic plane, the noise is due mainly to the confusion between different types of regions and to the fact that the atomic hydrogen component is not completely dominant in the IR map. Figure 5 shows the histogram of the values of σ all over the sky. The most probable value of σ is 40 × 10^{18} H cm^{-2} with a full width at half-maximum of 50 × 10^{18} H cm^{-2}. These values give an estimate of the detection level for IR-excess clouds and are in relative agreement with the errors in the initial surveys (see § II).

b) Definition of an Infrared-excess Cloud (IREC)

Our aim is to find the "significant" IR-excess clouds (hereafter IRECs) among the clouds that are defined by the 1 σ level. In the following, we define as connected two pixels with a side in common, and a 1 σ cloud as a set of connected pixels, each having a residual-to-noise ratio which is positive (i.e., corresponding to an IR excess) and above one. We choose σ as the estimate of the noise, though, in some cases it overestimates the true noise. The question can now be formulated as: how can we test that a 1 σ cloud is not simply a random fluctuation? In analogy with standard techniques in radioastronomy for the detection of lines appearing in more than one channel, we select first all the 1 σ clouds. The value of one σ seems reasonable in order to choose candidates. We then estimate the total noise ϕ of each complete cloud. If the residuals were independent from one pixel to another, the noise would increase with the size n (number of pixels) of the clouds as $\phi = n^{1/2}\sigma$, where σ is the rms of the residuals (assumed constant all over the cloud). However, both the northern and the southern H I surveys are not fully sampled so that adjacent pixels are not completely independent measurements of the sky. On the other hand, the adjacent pixels in the *IRAS* map are made of different scans, and are therefore independent measurements. Thus, a correction factor has to be applied to obtain the true value of the noise ϕ. In order to simplify the treatment of the data we decided to apply an all-sky correction of 1.5 to the noise which is equivalent to assume that the "effective" length after which the data are independent is 1/2°:

$$\phi = 1.5n^{1/2}\sigma \,. \tag{4.1}$$

We then define the significance S_g of the cloud candidate as the total signal-to-noise ratio:

$$S_g = \Sigma N_{\rm Hi}^e/\sigma_i/[\phi(n)/\sigma] = \tfrac{2}{3}n^{-1/2}\Sigma N_{\rm Hi}^e/\sigma_i \,, \tag{4.2}$$

where the sum runs over the n pixels inside the cloud.

Figure 6 shows a histogram of the significance S_g of the 1 σ clouds (*solid line*). The expected curve, if the map were purely noise, is shown as the dotted line. The excess over this curve

does indicate that high S_g cloud cannot have been generated by noise. Significances above 4 are practically absent in random maps, so that in order to construct a reliable catalog, the 1 σ clouds with a significance larger than 4 have been kept. Five hundred seventy-eight IRECs out of the 11,478 initial 1 σ clouds remained after this selection.

Figure 7 presents the map of the selected clouds. Beside the bright star-forming regions in the Galactic plane, the Orion-Taurus-Perseus molecular complex around $l \approx 180°$ and $b \approx -20°$ stands out very clearly. Extensions of this complex out to $b = -60°$ can be seen as first noticed from *IRAS* data by Magnani and Blitz (1985). The Ophiuchus complex above the Galactic plane is also in evidence at $l \approx 0°$ and $b \leq 20°$. Filaments of clouds are visible for $l \leq 180°$ in the northern Galactic hemisphere. These filaments are the most striking global features of this map. Some occur at constant Galactic longitudes, others seem to align with *IRAS* scans. As the method in § III corrects for baseline differences between *IRAS* scans, either there is indeed a filamentary structure in the IRECs or the gain of *IRAS* detectors was appreciably variable from one scan to another in this portion of the sky. Some caution should be applied to the clouds lying in the $(-30° \leq \delta \leq -25°)$ band where the two H I surveys overlap. As the two surveys do not match perfectly with each other, some spurious clouds can be induced.

c) *The Catalog of IRECs*

Among the 578 significant clouds, only those (516) outside the galactic plane ($|b_{II}| \geq 5°$) have been kept and ordered in increasing Galactic longitude in Table 1. Each cloud is

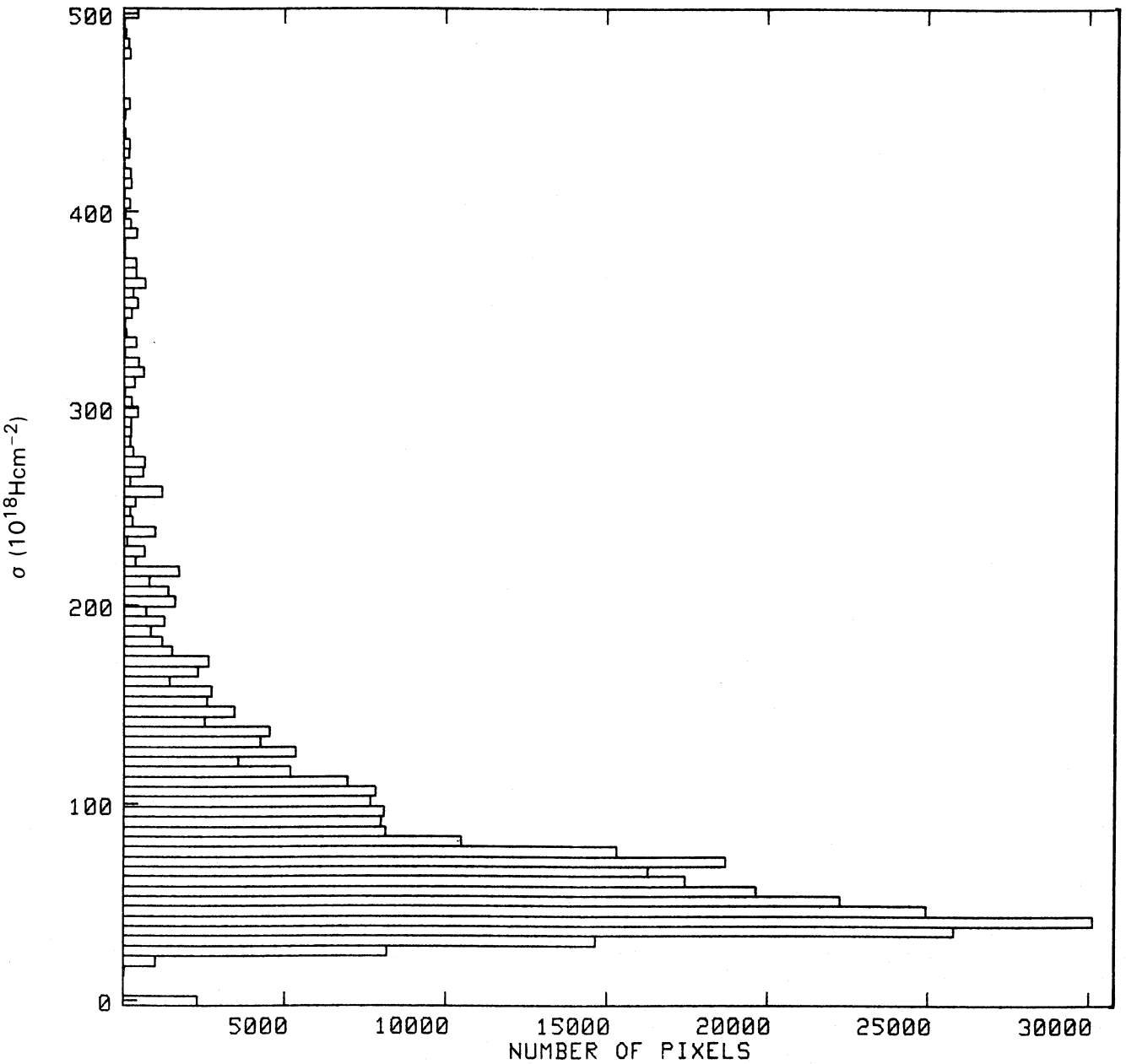

FIG. 5.—Histogram of the dispersion σ of the residues. The dispersion σ is on average lower in the northern hemisphere (main peak at 40×10^{18} H cm^{-2}) than in the southern hemisphere (secondary peak at 65×10^{18} H cm^{-2}).

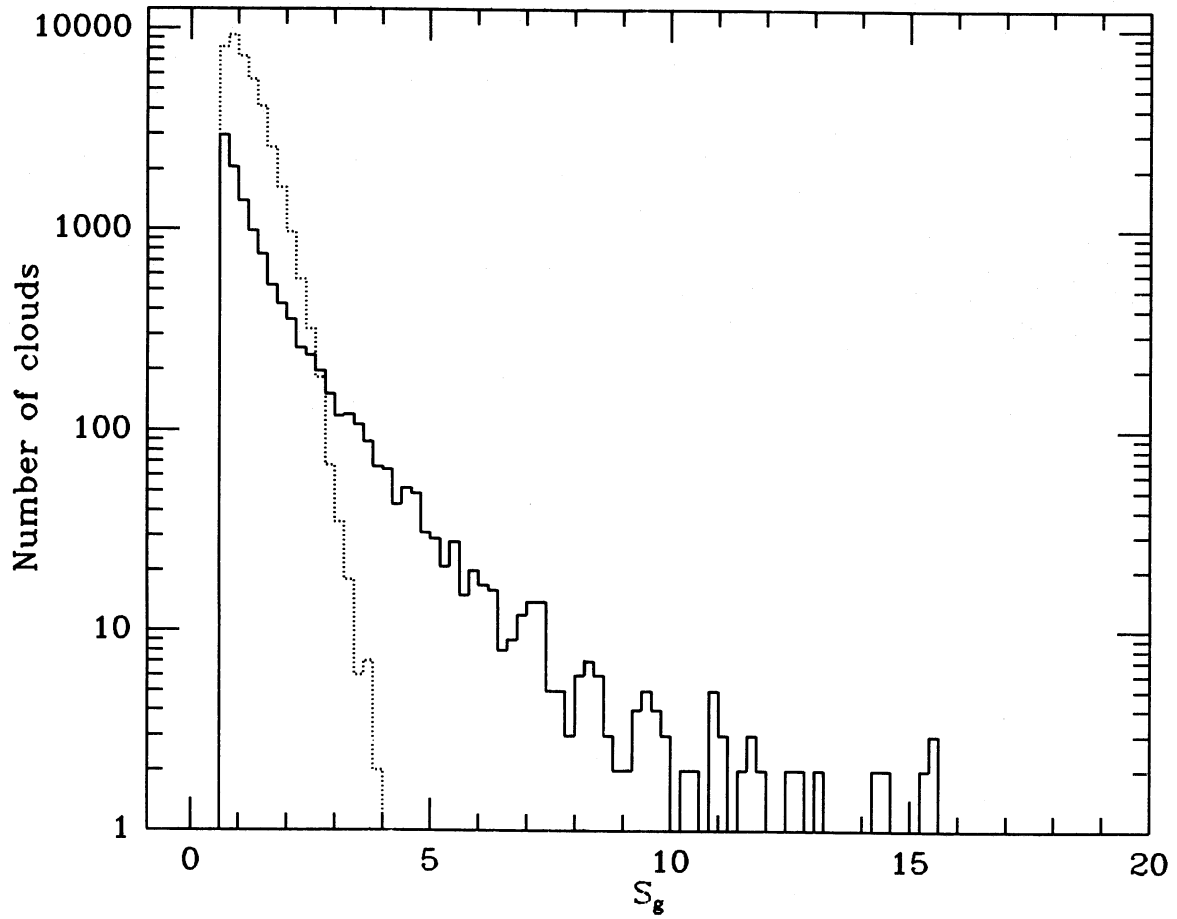

FIG. 6.—Histogram of the significance of the cloud candidates (*solid line*). Random map, following the reduced normal distribution and with the same size as the maps used in this work, produced the dotted line histogram. Above a significance of 4, very few clouds can be generated at random.

described as follows:

Column (*1*): The cloud number.

Column (*2*): The Galactic longitude l_{II}.

Column (*3*): The Galactic latitude b_{II} of the pixel with the maximum value of N_H^e/σ inside the cloud.

Column (*4*): The area in units of the pixels (each pixel covers 3.38×10^{-5} sr $= \frac{1}{9}$ deg^2).

Column (*5*): The significance S_g (formula [4.2]).

Column (*6*): The total hydrogen "mass flux" M/D^2 in units of $M_\odot/(100\text{ pc})^2$, where D is the (unknown) distance of the cloud in units of 100 pc:

$$(M_H^e/M_\odot)(D/100\text{ pc})^{-2} = 2.69 \times 10^{-3} \times \Sigma(N_H^e/10^{18}\text{ H cm}^{-2})\,, \quad (4.3)$$

where the sum is over the pixels inside the cloud. The mass is obtained by assuming the same ratio of IR-to-H I in the IREC as in the surrounding H I medium. It may be slightly underestimated if the IR-to–H I is actually lower in the IREC (see § V*c*). The inverse of the significance can be interpreted as an estimate of the uncertainty for the cloud mass flux (the mass M_H does not include helium and heavier elements).

Column (*7*): The average slope $S_{h4} = 1/\langle S_{4h}\rangle$ over the cloud, in units of MJy sr$^{-1}/10^{20}$ H cm^{-2}. An asterisk indicates that the correlation between H I and the IR is poor in the sense that the correlation coefficient computed in the cell C covering the cloud could be generated at random more than 5% of the time. However, the 31 clouds with an asterisk can still represent some interesting objects because they stand above the average IR emission in the surrounding region (delimited by the cell C). Negative numbers S_{h4} mean the failure of the correlation analysis. An association field with previously studied objects has been added, which is discussed in the following § IV*d*. We remark that in some cases (13%), the position of the maximum value of N_H^e inside a given IREC slightly differs from the one listed in Table 1, because the value of σ can vary in the cloud if it overlaps two cells C'. Some initial data that were estimated by interpolation are less accurate. Clouds which have been generated from these data, where the statistics may not be Gaussian anymore, have been marked in Table 1 ($\sim$10% of it) as GAPE, BHI, or BIR. They are probably less reliable because they are near missing data (in H I or IR) or coincide with bad H I or IR scans. Finally, we find that, using the same method as in § III but with H I as the independent variable, the clouds defined in Table 1 have their significance S_g increased by a median factor of 1.5 and their mass M_H^e by a factor 1.3. Therefore, the method used in § III has been rather stringent in selecting clouds.

b) Association with Known Objects

In order to associate a previously known object K with one of the clouds of Table 1, we test the values of the four pixels

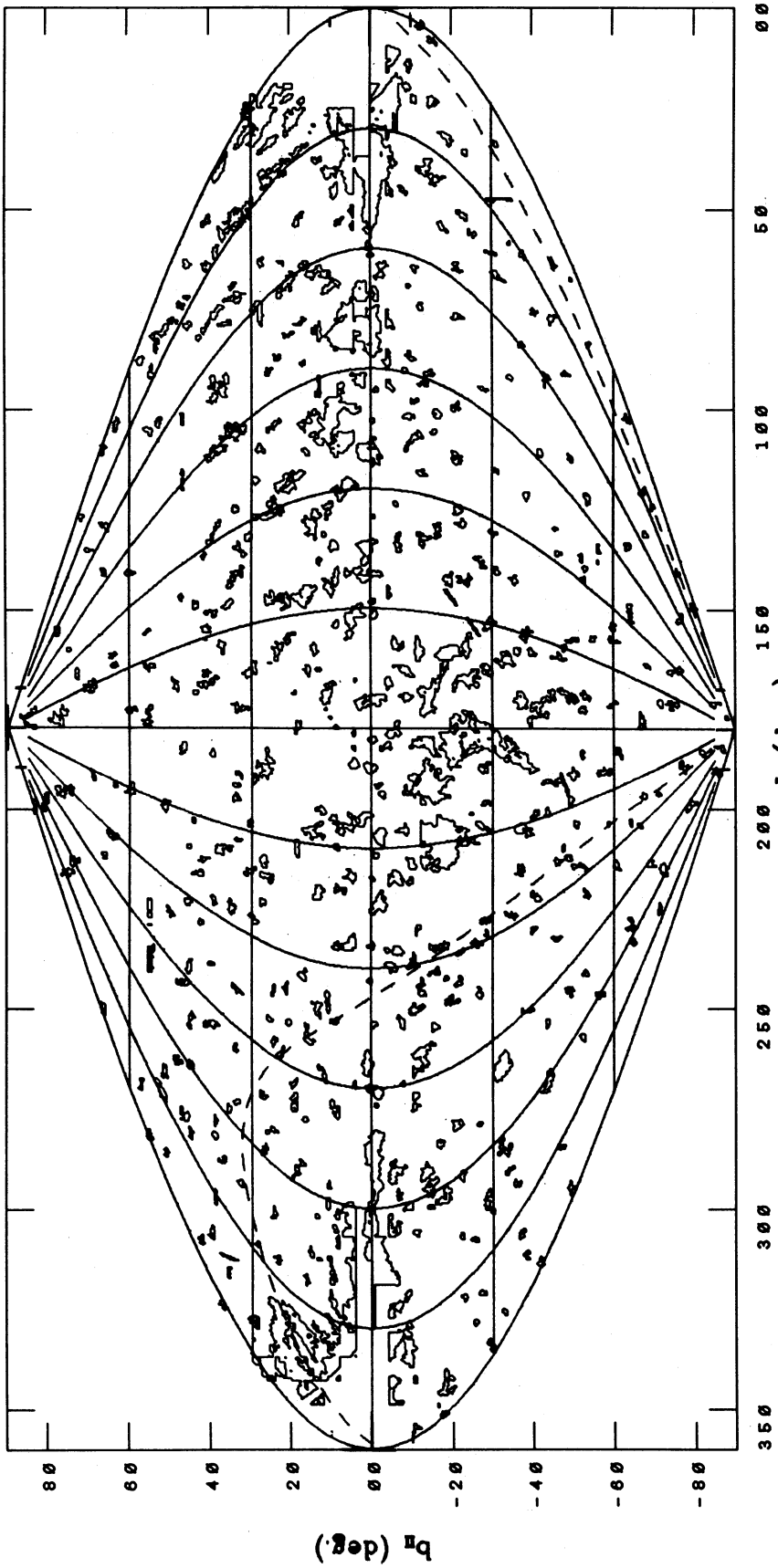

FIG. 7.—Map of the boundaries of the 578 IRECs that are significant at the level of $S_g = 4$. A few apparent defects remain in this map: (1) near the Galactic plane, especially near the Galactic center (i.e., $L < 50°$ or $L > 300°$), the limits of clouds are artificially at constant latitude (*horizontal lines*) due to a lack of H I data or to the shape of the cell C'; (2) few high-latitude clouds that have an horizontal linear shape can be spurious (for example, at $b_{II} = 54.^{\circ}7$ and $200° < L < 250°$ or at $b_{II} = 46.^{\circ}3$ and $100° < L < 125°$) because of bad H I scans, which the method in § III*b* failed to correct. Dashed line indicates the limit ($\delta = -30°$) between the two H I surveys that have been used (see § II*b*).

TABLE 1

SIGNIFICANT IRECs ($S_g \geq 4$) WITH $|b_{II}| \geq 5°$

Cloud (1)	l_{II} (2)	b_{II} (3)	Area (pixels)[a] (4)	S_g (5)	Mass[b] (6)	S_{h4}[c] (7)	Associations (8)
1.....	0°.05	−13°.00	13	26.	136.	9.8*	GAPE
2.....	1.36	−15.67	21	6.4	9.4	7.2*	
3.....	5.05	36.67	81	18.	41.	1.4	MBM36, 37
4.....	5.95	24.00	608	56.	318.	2.1*	S24 MBM57, 139, 145, 147, 148
5.....	6.42	−63.67	17	4.8	4.3	1.9*	
6.....	6.44	−49.67	5	4.2	2.3	1.4	
7.....	9.07	−31.33	12	4.9	4.8	1.1	
8.....	10.12	65.67	20	4.5	3.3	0.79	
9.....	11.10	−9.33	27	5.4	10.	11.*	GAPE
10.....	12.21	19.67	29	9.3	14.	4.1*	
11.....	12.61	41.00	12	4.1	3.4	1.2	
12.....	13.37	71.33	14	4.1	1.9	1.1	
13.....	13.40	40.33	15	4.0	3.9	1.2	
14.....	13.44	56.33	25	5.4	4.3	0.81	
15.....	14.07	−45.00	19	5.2	6.4	1.2	
16.....	14.17	62.33	25	6.7	5.9	0.63	
17.....	14.32	−79.33	13	4.6	2.4	16.*	GAPE
18.....	15.33	53.33	13	4.4	2.8	0.99	
19.....	16.11	16.67	18	6.1	5.4	3.5	
20.....	16.42	45.00	24	6.8	5.3	1.3	
21.....	16.67	−54.00	10	4.0	2.7	1.4	
22.....	17.48	−8.67	25	5.9	12.	12.*	
23.....	17.64	−15.67	43	6.3	13.	4.5	
24.....	18.72	24.00	64	11.	18.	1.8	MBM151
25.....	18.78	18.00	153	20.	66.	2.1	
26.....	18.79	−76.00	10	5.0	2.1	3.5*	
27.....	19.56	−10.67	21	4.4	8.5	12.	
28.....	19.80	−69.67	9	4.2	3.4	1.3	
29.....	21.26	52.33	22	4.5	3.8	0.96	
30.....	22.41	−23.67	17	4.5	5.0	1.7	
31.....	22.45	49.33	19	4.3	3.2	0.90	
32.....	22.87	50.00	37	7.2	8.4	0.83	
33.....	23.86	−67.67	18	5.1	4.6	2.6	
34.....	23.97	10.67	3	4.0	2.1	2.2	
35.....	24.56	46.67	19	4.0	3.2	0.93	
36.....	24.63	−20.00	46	7.0	16.	1.6	
37.....	24.94	13.67	4	4.8	3.0	2.2	
38.....	25.98	14.67	1	4.1	1.3	2.3	
39.....	26.68	−30.33	33	7.3	9.9	1.0	BIR
40.....	26.79	45.00	10	4.8	2.2	1.2	
41.....	26.88	54.00	26	5.7	5.7	0.84	
42.....	27.53	23.33	128	12.	32.	1.8	
43.....	27.95	40.67	32	5.3	5.6	3.1	
44.....	28.29	16.67	45	7.2	14.	2.1	
45.....	29.50	30.00	238	16.	56.	1.6	
46.....	29.67	−37.67	18	8.3	12.	1.5	BHI
47.....	30.93	37.67	28	5.0	6.0	2.0	
48.....	31.08	20.67	19	5.1	4.8	1.9	
49.....	31.25	−46.00	24	5.1	4.3	2.4	
50.....	32.07	−34.67	5	4.0	3.1	1.3	
51.....	34.07	13.33	22	4.2	11.	1.5	
52.....	36.39	−17.00	120	12.	53.	2.2	BIR
53.....	37.99	44.67	23	6.6	5.9	0.91	S73, MBM40
54.....	40.92	−22.67	30	5.4	9.2	1.5	
55.....	41.65	−30.67	16	4.5	4.2	1.1	
56.....	42.45	−40.67	15	4.1	2.6	1.4	
57.....	43.17	−25.67	17	4.2	3.9	1.1	
58.....	43.22	8.33	46	8.5	35.	2.0	
59.....	43.34	−8.00	19	4.4	8.9	1.9	
60.....	44.85	−49.00	13	4.9	2.9	1.4	
61.....	46.23	−31.00	33	6.0	8.7	1.2	
62.....	46.23	33.67	15	5.2	4.0	1.1	
63.....	46.71	17.67	34	5.4	13.	2.4	
64.....	47.43	42.33	13	4.3	3.3	1.1	
65.....	47.50	41.00	22	6.2	6.1	1.1	
66.....	47.76	−17.67	27	6.0	10.	2.1	
67.....	48.27	38.33	46	8.6	12.	1.2	
68.....	48.69	27.00	20	4.8	4.9	1.1	

TABLE 1—*Continued*

Cloud (1)	l_{II} (2)	b_{II} (3)	Area (pixels)[a] (4)	S_g (5)	Mass[b] (6)	S_{h4}[c] (7)	Associations (8)
69.....	50°.09	−68°.00	15	5.6	4.2	1.4	GAPE
70.....	50.50	69.67	12	4.0	1.8	1.2	
71.....	52.42	33.00	59	8.0	12.	1.1	
72.....	52.63	7.33	19	4.2	9.9	2.7	
73.....	52.97	54.00	25	4.9	3.5	0.79	
74.....	53.81	22.00	11	4.6	3.9	1.1	
75.....	55.38	35.33	23	4.6	4.4	1.3	
76.....	56.17	52.33	23	5.1	3.7	0.81	
77.....	56.33	−22.00	24	4.6	5.2	1.4	
78.....	57.88	−37.67	12	4.2	3.0	1.3	
79.....	58.43	16.33	30	6.0	9.9	1.2	
80.....	59.02	−43.33	25	6.3	7.0	1.4	
81.....	59.93	27.33	82	11.	22.	1.3	BHI
82.....	61.36	22.00	93	11.	27.	1.1	
83.....	61.48	−76.67	20	4.9	2.9	2.3	
84.....	62.51	−11.00	16	4.6	6.9	1.4	
85.....	63.15	64.67	24	4.8	3.6	1.1	
86.....	63.53	11.00	88	9.4	35.	1.5	
87.....	64.52	77.67	21	5.1	2.0	1.9	
88.....	67.40	−9.67	7	6.5	7.3	1.4	
89.....	67.96	10.00	63	7.1	29.	2.0	
90.....	68.00	46.33	18	6.0	3.6	0.97	BHI
91.....	68.38	−22.67	25	5.0	5.1	1.2	
92.....	71.72	35.33	25	5.4	5.3	1.2	
93.....	72.52	−12.33	18	4.8	7.0	1.2	
94.....	73.01	−34.67	15	4.2	3.2	1.9	GAPE
95.....	73.20	16.00	19	4.3	4.4	1.4	
96.....	74.03	36.67	122	12.	29.	2.0	
97.....	74.21	−50.00	15	4.0	2.7	1.7	
98.....	75.13	20.33	17	4.2	4.4	0.93	
99.....	75.75	−86.33	19	5.0	3.0	7.5*	
100.....	76.76	−63.33	19	4.1	2.7	1.2	
101.....	79.22	22.67	17	4.7	4.0	0.92	
102.....	79.34	12.33	49	7.7	37.	0.95	
103.....	80.70	25.00	17	4.5	3.6	1.1	
104.....	80.84	66.00	15	4.5	2.2	1.3	
105.....	82.46	−54.00	27	5.5	5.1	1.5	
106.....	83.73	−28.00	14	4.3	3.1	1.2	
107.....	84.66	16.67	12	4.6	4.8	0.76	
108.....	85.49	−11.33	22	5.5	13.	1.4	
109.....	85.76	−42.33	20	5.2	4.3	1.8	
110.....	87.31	−14.67	23	4.8	8.4	1.6	
111.....	87.79	46.33	10	5.9	2.3	0.97	BHI
112.....	88.70	−8.33	13	4.3	7.8	1.4	
113.....	89.92	38.67	88	12.	23.	0.73	MBM41–44
114.....	90.26	12.33	33	7.1	24.	1.3	
115.....	90.45	32.33	35	6.9	9.6	1.2	
116.....	90.48	35.00	88	9.4	18.	1.2	
117.....	90.55	−14.33	20	4.0	6.6	1.8	
118.....	90.69	46.33	9	5.9	2.2	0.97	BHI
119.....	92.62	46.33	5	4.2	1.2	0.97	BHI
120.....	93.36	−22.00	26	5.3	6.7	1.1	
121.....	94.58	−5.67	27	12.	71.	1.5	S125
122.....	96.03	−11.33	15	4.3	7.1	1.6	
123.....	97.39	25.33	36	5.9	10.	1.3	
124.....	98.23	−16.67	32	5.8	11.	1.6	
125.....	98.67	9.00	497	47.	1360	1.3	H:CEP OB2
126.....	98.82	−56.33	11	4.1	2.6	1.3	
127.....	99.03	12.67	18	4.4	9.9	1.2	S130
128.....	99.94	15.00	49	7.4	27.	1.2	
129.....	100.45	27.33	28	5.8	8.3	1.3	
130.....	100.88	−9.67	28	4.6	10.	1.6	
131.....	102.23	59.33	20	7.3	3.5	1.2	M101
132.....	102.67	−16.00	14	4.2	5.4	1.8	
133.....	103.97	14.33	14	11.	31.	1.2	
134.....	104.24	−56.33	3	4.5	1.5	1.3	
135.....	104.56	−31.00	10	4.2	2.5	2.3	
136.....	104.70	74.33	8	4.4	1.2	1.8	N5055
137.....	105.46	−11.67	58	8.2	25.	1.3	
138.....	105.70	−20.33	19	4.7	4.8	1.2	
139.....	105.72	−38.67	21	6.1	4.5	2.1	

TABLE 1—*Continued*

Cloud (1)	l_{II} (2)	b_{II} (3)	Area (pixels)[a] (4)	S_g (5)	Mass[b] (6)	S_{h4}[c] (7)	Associations (8)
140.....	106°31	−87°67	7	4.9	2.2	18.*	N253
141.....	106.72	5.00	215	40.	1340.	1.2	S140, 145
142.....	107.18	16.00	19	4.1	12.	2.0	
143.....	107.54	−46.00	6	6.8	3.0	1.4	
144.....	108.43	−21.33	24	4.8	5.6	1.2	
145.....	108.58	28.67	23	4.9	6.0	1.7	
146.....	109.07	−52.00	12	4.5	3.7	1.5	
147.....	112.32	−64.00	34	7.3	7.3	1.2	
148.....	112.46	−53.33	12	4.0	3.5	1.4	
149.....	112.96	17.33	118	11.	53.	2.9	MBM161, 162
150.....	113.92	33.67	22	4.5	4.6	1.7	
151.....	114.49	−12.33	23	5.2	7.8	1.0	
152.....	115.15	37.67	18	4.6	3.8	0.85	BIR
153.....	115.70	−46.00	14	4.1	2.7	1.5	
154.....	115.79	20.00	40	6.0	17.	2.	MBM163–165
155.....	117.89	−52.67	12	4.1	3.6	1.4	MBM2
156.....	118.17	24.33	29	4.6	8.2	2.7	
157.....	119.38	39.67	24	5.0	4.5	0.93	BIR
158.....	119.96	27.33	61	8.7	20.	2.3	BHI
159.....	121.04	22.00	26	5.2	11.	3.2	
160.....	121.18	−21.67	27	16.	17.	1.1	M31, M32
161.....	122.29	41.33	10	4.0	2.1	1.2	BIR
162.....	122.45	−31.00	15	4.0	2.6	1.1	
163.....	122.86	9.67	47	6.4	35.	1.1	
164.....	123.32	−6.33	10	15.	54.	1.3	S184
165.....	123.81	30.00	25	5.7	9.7	1.5	
166.....	124.64	−22.00	28	5.5	6.3	1.9	
167.....	125.75	32.67	35	6.2	10.	1.2	
168.....	126.92	−74.33	30	6.4	5.4	1.1	
169.....	127.20	−59.67	17	4.0	2.6	1.1	
170.....	127.46	−16.67	35	5.5	9.7	1.3	
171.....	127.71	14.33	126	13.	101.	1.3	
172.....	129.97	11.67	10	4.4	12.	1.1	
173.....	131.08	−13.00	44	7.0	20.	1.1	
174.....	131.43	46.67	12	4.6	2.5	1.6	
175.....	131.51	−26.67	11	4.4	2.6	1.1	
176.....	132.22	31.67	34	5.3	6.8	1.2	
177.....	133.43	9.00	40	9.7	44.	1.6	
178.....	133.57	−28.00	17	4.0	3.1	1.0	
179.....	133.69	−6.67	43	6.0	29.	1.4	H:PER OB1
180.....	133.72	−31.00	18	14.	11.	0.93	M33
181.....	134.13	72.67	22	5.4	2.9	2.2	BIR
182.....	134.46	−35.67	23	5.5	5.1	0.97	
183.....	134.57	34.00	28	5.1	6.2	1.1	
184.....	135.78	−59.67	15	4.5	2.6	1.1	
185.....	136.27	12.67	13	4.2	9.1	1.3	
186.....	136.77	54.67	10	5.2	1.9	0.94	
187.....	137.16	43.00	21	4.7	3.7	1.6	
188.....	137.29	−68.00	11	5.6	3.6	1.2	
189.....	138.15	63.00	14	4.3	1.9	1.5	N4088
190.....	139.80	83.33	13	4.6	2.0	1.1	
191.....	140.12	−24.33	40	6.1	9.7	1.2	
192.....	140.21	8.67	48	7.1	40.	2.5	
193.....	140.79	6.00	19	4.2	27.	1.4	
194.....	141.06	−55.00	13	4.1	2.4	1.3	
195.....	141.33	40.67	7	9.5	4.5	1.6	M81, M82
196.....	141.57	−19.00	44	6.5	14.	1.7	
197.....	141.59	35.33	33	9.8	11.	0.91	MBM27, 28, 29
198.....	142.87	84.33	19	5.2	3.0	1.3	N4631
199.....	143.03	38.33	18	4.5	4.2	1.3	MBM30
200.....	143.34	−19.00	26	5.8	10.	1.4	BIR
201.....	143.41	10.33	53	7.2	42.	2.2	
202.....	143.93	63.67	15	4.0	1.7	0.94	
203.....	144.69	25.00	114	11.	30.	1.2	
204.....	146.01	−49.67	22	6.0	5.2	1.6	MBM5
205.....	146.60	16.67	160	13.	97.	1.3	
206.....	147.20	40.33	25	6.0	5.5	1.7	MBM32
207.....	147.45	69.00	53	7.7	8.2	3.4	
208.....	148.16	−29.67	18	4.1	4.8	1.3	
209.....	148.98	−38.33	18	4.5	4.7	1.3	
210.....	150.00	−24.33	9	5.3	5.6	1.5	BIR

TABLE 1—*Continued*

Cloud (1)	l_{II} (2)	b_{II} (3)	Area (pixels)[a] (4)	S_g (5)	Mass[b] (6)	S_{h4}[c] (7)	Associations (8)
211.....	150°.12	40°.67	2	4.5	1.1	1.6	
212.....	150.18	−29.33	25	5.0	7.2	1.3	
213.....	150.30	−47.67	15	4.0	3.2	1.4	
214.....	150.45	55.67	25	5.8	2.9	1.3	
215.....	150.81	−38.00	14	4.5	4.7	1.2	MBM7
216.....	151.23	−25.33	15	5.0	6.4	1.4	BIR
217.....	153.05	8.33	21	5.3	17.	1.6	
218.....	153.29	37.00	33	6.8	7.1	2.1	
219.....	153.66	−24.33	12	5.7	6.8	1.5	
220.....	153.93	−47.33	26	6.0	6.3	1.3	
221.....	154.45	−39.67	22	7.2	9.3	1.2	
222.....	154.99	−75.33	29	4.9	4.3	0.83	
223.....	155.57	5.00	26	4.6	29.	1.5	
224.....	155.67	21.33	29	4.7	7.9	2.0	
225.....	156.20	−35.67	22	4.6	6.1	1.3	
226.....	157.35	22.00	54	6.5	13.	1.9	
227.....	158.21	−6.00	49	6.8	42.	1.5	
228.....	158.70	14.00	28	6.1	13.	1.8	
229.....	158.77	−33.67	86	18.	51.	1.5	MBM12
230.....	159.55	−12.00	77	19.	97.	3.8*	
231.....	159.90	−19.00	211	44.	316.	2.5*	H: PER OB2 MBM101–104
232.....	160.21	−71.33	19	4.6	4.4	1.0	
233.....	161.20	40.33	19	4.7	3.0	1.1	
234.....	161.61	25.00	3	5.2	2.3	0.87	
235.....	162.09	−18.33	45	6.8	29.	1.5	S220
236.....	162.52	−28.67	49	7.2	20.	1.7	
237.....	162.90	28.67	57	7.7	9.8	1.4	
238.....	163.06	48.00	24	4.6	2.9	3.7	BIR
239.....	163.70	39.00	17	4.6	3.0	1.8	
240.....	164.10	15.33	24	4.8	8.0	1.5	
241.....	164.60	13.00	9	7.9	8.6	1.7	
242.....	165.13	40.33	32	6.1	5.1	1.1	
243.....	165.15	−9.00	59	13.	67.	2.7	S222
244.....	166.46	−48.33	25	5.7	7.6	1.2	
245.....	166.46	−24.33	143	28.	190.	1.4	MBM17
246.....	166.67	−60.00	12	4.3	2.5	1.1	
247.....	167.10	43.67	11	4.4	2.1	0.99	
248.....	167.52	−54.00	25	4.9	4.3	0.93	
249.....	169.33	−49.00	36	5.8	8.2	1.0	
250.....	169.94	58.00	23	4.7	3.5	1.0	
251.....	170.15	18.67	5	4.6	2.4	0.83	
252.....	171.16	−37.67	84	19.	61.	1.2	MBM16
253.....	171.57	−8.67	37	7.4	31.	2.2	
254.....	172.16	12.00	93	9.9	56.	1.9	
255.....	172.36	34.00	19	4.5	2.7	1.7	
256.....	172.42	−52.00	21	5.4	5.0	0.89	N1068, N1055
257.....	173.11	76.00	81	8.9	15.	4.2*	
258.....	173.76	31.33	17	4.1	2.8	1.3	MBM25
259.....	173.79	−41.33	101	13.	43.	1.2	
260.....	174.17	−13.67	224	24.	287.	1.3	
261.....	174.53	83.00	22	5.0	3.0	1.1	N4414, 4395
262.....	174.91	11.00	3	4.5	4.6	1.5	
263.....	175.42	−43.33	16	4.4	5.9	0.99	
264.....	175.93	55.00	46	6.4	8.1	1.8*	
265.....	176.95	10.00	4	4.0	4.8	1.3	
266.....	177.44	−67.00	36	6.1	5.5	0.87	
267.....	178.70	−39.67	23	7.5	13.	1.1	
268.....	178.99	−6.33	15	4.2	14.	1.6	
269.....	179.30	18.00	28	7.2	12.	0.68	
270.....	179.66	8.67	8	9.9	16.	1.3	
271.....	181.34	−5.00	51	7.4	52.	1.4	
272.....	186.24	−16.00	149	14.	94.	2.2	S246
273.....	186.72	46.00	30	6.5	5.2	3.8	BIR
274.....	188.23	39.67	17	4.9	3.1	2.3	
275.....	189.63	−61.00	23	4.8	3.8	1.1	
276.....	189.93	−36.33	1215	76.	911.	1.3	MBM18, 19, 106–109
277.....	191.13	−16.67	11	6.1	7.9	1.6	
278.....	191.40	25.00	108	11.	26.	0.70	
279.....	191.46	−52.33	13	5.5	4.2	0.87	MBM15

TABLE 1—*Continued*

Cloud (1)	l_{II} (2)	b_{II} (3)	Area (pixels)[a] (4)	S_g (5)	Mass[b] (6)	S_{h4}[c] (7)	Associations (8)
280.....	191°70	−28°00	40	7.4	12.	1.4	
281.....	192.92	28.67	22	4.6	4.4	0.99	
282.....	193.12	33.00	13	5.4	3.4	1.1	
283.....	194.94	−16.33	523	59.	754.	2.1	S263, 265
284.....	196.69	33.00	14	4.5	2.7	1.2	
285.....	196.77	−49.00	37	6.3	9.6	1.1	
286.....	199.84	−56.33	37	7.2	7.7	0.69	
287.....	200.67	33.00	21	4.5	3.3	1.2	
288.....	200.76	−28.00	18	4.4	5.4	1.4	
289.....	201.47	12.00	29	5.8	11.	2.2	
290.....	202.61	9.00	30	4.6	12.	1.9	
291.....	203.07	−48.33	68	8.3	19.	1.1	BIR
292.....	203.11	−24.67	5	6.1	4.5	1.9	
293.....	204.29	13.00	87	10.	24.	2.0	
294.....	205.56	−7.67	36	5.2	35.	6.5	
295.....	206.41	−26.33	35	11.	21.	1.7	MBM21, 22
296.....	206.94	30.00	17	5.4	3.6	1.4	
297.....	207.44	−49.00	21	7.3	8.5	1.0	
298.....	208.20	50.33	31	5.5	3.9	1.1	
299.....	208.72	−40.00	21	4.7	4.3	1.1	
300.....	208.86	−20.67	937	154.	5170	1.8	H:ORI OB1 S279, 281 MBM110, 111
301.....	209.85	18.33	36	8.5	15.	1.0	BHI
302.....	209.95	−43.67	19	4.2	3.2	1.1	
303.....	210.04	9.00	16	4.1	6.3	2.4	
304.....	210.13	58.67	30	7.1	5.5	1.0	
305.....	210.75	−36.67	49	14.	26.	1.6	MBM20
306.....	210.84	63.00	9	4.1	1.7	1.1	
307.....	211.60	68.33	18	4.7	3.0	1.1	GAPE
308.....	211.80	43.67	8	5.4	2.6	1.2	
309.....	212.99	33.00	11	4.4	2.4	1.1	BIR
310.....	214.38	−40.00	22	4.4	4.4	1.9	
311.....	214.49	−9.67	41	5.4	38.	−30.	
312.....	216.07	34.67	58	8.5	10.	1.1	
313.....	216.51	−5.67	87	9.0	98.	3.0	
314.....	216.81	−50.67	16	4.4	3.6	1.1	
315.....	217.04	27.00	40	8.0	9.0	0.90	
316.....	217.48	5.00	43	7.2	30.	1.6	
317.....	219.15	−9.00	17	4.2	15.	5.1	
318.....	220.61	6.67	30	4.7	14.	1.9	
319.....	221.05	25.67	41	7.0	7.6	0.95	BIR
320.....	221.48	45.00	9	9.2	5.0	2.0	IRC10216
321.....	221.57	30.00	29	6.3	5.7	1.1	
322.....	223.10	13.00	59	8.4	19.	1.7	
323.....	223.95	41.33	17	4.1	2.8	2.0	
324.....	224.11	−67.33	14	5.1	4.5	1.1	
325.....	224.26	−47.33	10	4.6	3.0	1.1	
326.....	224.66	−37.00	30	5.8	8.1	2.1	
327.....	225.51	−58.67	6	4.0	2.2	1.1	
328.....	228.10	−78.00	29	5.8	6.5	1.2	
329.....	228.46	−46.00	17	4.5	5.9	1.9	
330.....	228.78	−49.00	20	4.3	5.2	2.1	
331.....	229.01	27.00	18	4.3	2.8	0.97	
332.....	229.87	42.67	25	4.7	3.8	1.8	
333.....	230.17	−71.00	7	4.2	2.7	0.98	
334.....	231.62	−11.00	16	4.2	12.	1.0	
335.....	231.71	−64.00	10	4.0	3.5	1.4	
336.....	233.12	35.33	35	5.2	4.7	1.2	
337.....	233.61	−28.00	23	4.7	5.8	1.4	
338.....	234.39	−40.00	30	7.0	13.	3.2*	BHI
339.....	234.90	39.00	18	7.4	5.2	1.4	
340.....	235.09	28.67	24	4.9	3.7	1.1	
341.....	235.59	8.33	23	4.4	13.	1.7	
342.....	235.97	−6.00	43	8.0	67.	2.1	S310
343.....	236.19	−52.33	30	5.9	9.1	1.7	
344.....	236.42	−14.33	22	5.0	14.	1.2	
345.....	236.69	−34.00	24	6.4	9.3	2.5	BHI
346.....	236.89	73.67	17	4.8	3.0	1.4	
347.....	237.27	−17.33	29	4.7	11.	0.92	
348.....	237.41	−83.67	32	7.0	8.1	1.3*	

TABLE 1—*Continued*

Cloud (1)	l_{II} (2)	b_{II} (3)	Area (pixels)[a] (4)	S_g (5)	Mass[b] (6)	S_{b4}[c] (7)	Associations (8)
349.....	237°.94	−10°.33	35	6.0	28.	1.7	H:Co11121
350.....	238.52	−28.00	9	4.2	4.0	0.75	BHI
351.....	239.21	−25.00	28	6.9	12.	0.62	BHI
352.....	240.12	−21.33	17	8.2	13.	0.85	BHI
353.....	240.21	63.00	13	4.8	2.6	0.92	N3593
354.....	240.81	45.00	20	4.5	3.1	0.86	
355.....	242.28	−67.00	9	4.0	3.2	1.3	
356.....	242.32	64.67	15	4.8	2.7	1.0	N3627, 3628
357.....	242.52	−16.33	23	5.5	17.	2.3	BHI
358.....	244.57	−12.67	19	4.5	15.	2.4	
359.....	244.83	17.00	32	8.2	15.	1.2	
360.....	245.04	42.00	12	4.0	2.3	1.4	
361.....	245.48	−40.67	14	4.1	4.9	3.2*	
362.....	245.79	−18.67	9	8.4	13.	2.3	
363.....	246.49	76.67	19	4.7	2.7	1.5	
364.....	247.32	75.67	20	4.7	3.0	1.4	
365.....	247.56	−12.33	22	7.1	25.	2.3	
366.....	247.69	20.67	18	5.7	6.5	1.2	
367.....	248.04	−60.67	22	5.5	7.1	1.4	
368.....	248.10	−53.33	17	4.0	4.9	1.7	
369.....	248.40	−20.67	23	5.1	10.	1.6	
370.....	250.04	49.67	19	5.4	4.0	0.94	GAPE
371.....	250.21	10.67	41	9.8	34.	1.1	BHI
372.....	250.82	13.00	43	7.4	30.	0.83	
373.....	250.97	24.33	17	4.6	4.6	0.93	
374.....	251.22	−12.00	48	9.5	56.	1.9	
375.....	252.21	−19.67	36	5.8	16.	2.5	
376.....	253.27	−7.33	32	6.6	74.	1.9	
377.....	253.57	9.00	20	4.0	11.	1.0	
378.....	254.53	−86.67	19	4.5	3.9	9.5*	
379.....	254.82	−27.00	24	5.6	11.	1.0	
380.....	255.82	−46.00	15	4.2	4.2	1.3	
381.....	256.58	40.00	12	4.4	2.6	0.99	
382.....	257.04	66.00	14	4.5	2.3	0.97	
383.....	257.10	34.33	24	6.2	6.2	0.91	GAPE
384.....	257.77	−15.33	25	5.5	18.	2.3	
385.....	257.81	54.67	26	7.5	12.	0.95	BHI
386.....	258.38	20.67	15	4.1	4.7	1.1	
387.....	259.06	16.00	45	7.1	24.	1.0	
388.....	260.18	25.00	14	4.8	4.2	1.0	GAPE
389.....	261.27	54.67	12	5.6	6.3	0.95	BHI
390.....	262.23	−12.33	146	14.	177.	3.2*	
391.....	263.44	45.00	31	6.4	5.5	0.92	
392.....	264.73	54.67	3	4.7	2.1	1.1	BHI
393.....	265.38	24.00	20	4.6	5.0	0.92	
394.....	266.67	13.33	30	6.0	16.	1.3	
395.....	268.14	22.67	24	5.6	8.6	1.0	
396.....	268.46	−37.33	20	4.3	6.5	1.0	
397.....	268.86	−8.00	8	5.1	35	15.*	
398.....	271.10	45.67	29	6.9	5.5	0.90	
399.....	273.15	−11.33	24	5.5	15.	1.7	
400.....	273.76	54.33	50	8.7	14.	1.1	BHI
401.....	273.91	38.33	39	7.0	6.4	1.1	
402.....	273.94	−69.00	22	4.9	10.	3.6*	
403.....	274.13	19.00	21	4.2	8.7	0.99	
404.....	274.34	9.67	18	4.2	9.4	1.0	
405.....	275.79	33.00	16	4.4	2.9	1.0	
406.....	275.87	18.33	22	4.7	11.	1.2	
407.....	275.89	−10.33	20	5.5	14.	1.7	
408.....	277.29	9.33	26	4.7	13.	1.0	
409.....	278.28	−48.33	24	5.7	7.8	1.2	
410.....	280.36	−43.33	16	4.2	7.0	0.91	BIR
411.....	280.54	−33.33	178	80.	846.	1.5	LMC
412.....	280.83	19.00	29	6.2	17.	1.2	
413.....	281.36	−53.00	15	4.6	5.2	0.93	
414.....	281.43	16.33	14	5.7	10.	1.3	
415.....	281.46	26.67	20	5.4	6.8	1.4	
416.....	282.30	45.00	27	5.5	4.3	1.1	
417.....	284.07	−79.67	32	7.3	14.	5.3*	
418.....	285.70	−22.00	45	7.9	38.	1.1	
419.....	288.75	−17.00	25	4.5	18.	2.0	

TABLE 1—*Continued*

Cloud (1)	l_{II} (2)	b_{II} (3)	Area (pixels)[a] (4)	S_g (5)	Mass[b] (6)	S_{h4}[c] (7)	Associations (8)
420.....	290°.36	−27°.00	9	4.8	7.1	1.1	
421.....	290.76	72.67	30	6.1	4.6	1.3	
422.....	290.89	33.00	14	4.9	3.1	1.3	
423.....	291.32	25.67	25	4.5	6.8	1.9	
424.....	292.18	−64.67	10	4.3	3.6	1.2	
425.....	293.49	17.33	15	4.8	8.7	1.4	
426.....	294.06	−64.00	15	4.8	5.3	1.1	
427.....	294.40	−14.00	71	8.8	48.	2.5	KM15, 16
428.....	295.33	−72.33	36	5.9	19.	3.1*	
429.....	296.04	35.33	15	4.5	2.9	1.3	
430.....	296.34	10.67	11	4.3	8.7	1.2	
431.....	296.71	18.00	24	4.3	11.	1.2	
432.....	297.36	−15.67	76	9.5	51.	2.4	
433.....	297.80	−6.67	19	4.4	9.6	2.2	
434.....	298.24	26.67	24	4.8	6.9	1.3	
435.....	299.27	45.00	22	4.9	3.4	1.4	
436.....	300.26	−56.33	22	5.9	7.1	1.1	
437.....	300.29	−22.67	25	5.3	15.	2.7	
438.....	301.05	−9.67	29	6.5	17.	3.0	
439.....	301.09	10.67	24	6.8	19.	1.2	BHI
440.....	301.46	81.00	35	5.6	4.6	1.2	
441.....	302.05	48.00	24	5.4	4.4	2.0	
442.....	302.23	−19.33	75	8.6	35.	3.9	
443.....	302.36	−64.33	18	4.9	6.1	1.2	
444.....	303.26	−44.00	64	15.	48.	2.0	SMC
445.....	303.89	−15.00	12	4.3	8.3	2.3	
446.....	304.54	−31.67	7	6.7	7.9	1.7	
447.....	305.04	13.33	8	5.2	7.8	1.3	N4945
448.....	305.09	38.67	14	4.3	3.0	1.4	
449.....	305.60	−33.00	36	6.2	16.	1.6	
450.....	305.94	−34.33	12	5.5	8.0	1.5	
451.....	306.22	9.00	16	4.4	10.	1.3	
452.....	307.52	−52.67	16	4.8	5.4	1.9	
453.....	308.02	−11.00	19	5.9	13.	3.6	
454.....	309.60	8.00	20	4.9	14.	2.1	
455.....	309.78	38.67	20	6.6	5.6	1.5	
456.....	312.63	−29.00	56	8.9	25.	1.5	
457.....	313.49	36.00	17	5.0	3.0	1.6	
458.....	313.77	−33.67	18	4.1	6.6	1.3	
459.....	313.89	24.33	19	4.7	6.9	1.5	
460.....	314.52	32.33	20	6.9	5.2	1.1	N5236
461.....	315.07	14.67	19	4.9	9.3	1.7	
462.....	315.78	74.33	31	4.5	3.5	1.3	
463.....	316.13	51.00	30	6.2	6.1	2.1	
464.....	316.16	13.00	7	4.1	4.8	1.7	
465.....	316.97	−22.00	11	4.2	5.8	1.5	
466.....	317.49	9.33	26	7.2	20.	2.8	
467.....	318.43	46.67	12	6.4	4.0	1.1	
468.....	318.71	9.00	23	6.7	17.	3.3	
469.....	319.50	−35.67	20	4.6	7.4	1.1	
470.....	320.86	−25.00	13	4.7	6.3	1.3	
471.....	321.29	−71.00	16	5.6	8.9	0.88	GAPE
472.....	321.83	16.00	15	4.6	7.4	1.8	
473.....	322.60	44.33	18	4.5	3.6	1.2	
474.....	322.72	47.00	26	5.6	5.3	1.1	
475.....	323.77	−9.00	26	4.1	15	−15.*	
476.....	323.77	22.67	18	4.3	7.2	1.6	
477.....	324.58	51.33	53	32.	174.	1.9	Saturn
478.....	325.72	28.00	12	4.0	3.9	1.1	
479.....	325.93	9.33	37	7.0	20.	9.9	
480.....	327.35	8.67	11	4.7	6.4	7.1*	
481.....	329.42	38.67	18	4.7	3.6	1.2	
482.....	333.95	−47.33	15	4.3	4.5	1.4	
483.....	334.26	−23.00	16	5.5	7.6	1.5	
484.....	334.50	13.33	18	4.5	8.4	2.3	
485.....	335.40	12.00	39	9.8	29.	3.2*	
486.....	338.16	−26.67	16	4.5	5.5	1.6	
487.....	338.60	−37.00	22	4.4	5.8	1.0	
488.....	341.91	82.67	23	5.5	3.7	1.2	BHI
489.....	342.47	−86.00	19	4.8	4.8	3.2	
490.....	342.99	39.00	26	5.5	5.4	1.4	

TABLE 1—*Continued*

Cloud (1)	l_{II} (2)	b_{II} (3)	Area (pixels)[a] (4)	S_g (5)	Mass[b] (6)	S_{h4}[c] (7)	Associations (8)
491.....	344°15	36°67	21	5.0	4.7	1.2	
492.....	344.55	8.67	9	13.	32.	1.7*	
493.....	344.64	57.00	16	5.2	3.1	0.94	
494.....	345.02	50.33	16	4.5	3.4	1.5	
495.....	345.04	−26.00	13	4.4	4.7	2.0	
496.....	345.53	−10.67	13	4.4	9.9	−16.*	BHI
497.....	346.30	35.33	13	4.1	3.6	1.3	
498.....	346.33	−37.67	18	4.6	5.5	1.2	
499.....	349.00	29.33	38	6.2	12.	2.0	
500.....	349.22	16.00	1410	111.	1840	2.3*	H:SCO OB2 MBM113–115, 117–124
501.....	349.59	−18.67	32	34.	215.	3.0	BIR
502.....	350.01	41.67	19	4.2	3.6	1.9	
503.....	352.05	−18.67	66	40.	571.	3.5	BIR
504.....	353.74	66.00	24	5.5	3.1	2.0	
505.....	354.17	29.00	3	4.7	2.5	1.6	
506.....	354.35	14.67	42	8.2	27.	12.*	
507.....	354.36	22.00	3	4.8	3.4	4.9	
508.....	354.75	−33.33	13	5.2	5.3	2.0	BHI
509.....	354.94	−49.33	22	4.5	5.7	1.5	
510.....	355.12	−29.33	25	5.4	8.0	1.2	
511.....	355.79	54.67	23	4.3	4.1	2.0	
512.....	356.11	−16.33	3	7.7	7.7	5.3	BIR
513.....	357.74	−10.67	17	4.7	9.3	−16.*	
514.....	359.01	−42.33	18	4.1	4.3	0.97	
515.....	359.11	36.67	15	6.7	5.7	1.4	MBM33
516.....	359.81	−17.67	11	4.1	8.1	6.9	BIR

[a] A pixel is $\frac{1}{9}$ deg^2.

[b] The unit of equivalent hydrogen excess mass is $M_\odot/(100\ \mathrm{pc})^2$.

[c] The unit of the IR-to-H I ratio S_{h4} (deduced from the correlation analysis as the inverse of the slope S_{4h}) is MJy sr^{-1}/(10^{20} H cm^{-2}).

NOTES.—Asterisk (*) means the correlation between the IR and H I data is weak or absent and could be random in more than 5% of the cases.

Key to col. (8) is as follows: BHI: bad H I scan or H I defect. BIR: bad IR scan or IR defect. GAPE: gap edge in H I or IR data. H: H II regions; Humphreys 1978. KM: high-latitude molecular clouds; Keto and Myers 1986. MBM: High-latitude molecular clouds; Magnani, Blitz, and Mundy 1985. M: Messier external galaxies. N: NGC external galaxies. S: Sharpless H II regions; Blitz, Fich, and Stark 1982.

nearest to the center of the object *K*. At least two of the 4 nearest pixels or the nearest pixel to the center of the object *K* must lie inside the IREC for the cloud to be associated with *K*. A representative rather than exhaustive list of catalogs of objects has been searched for association with the clouds of Table 1. The list includes: (1) the high-latitude CO surveys by MBM and KM; (2) some high-velocity H I surveys; (3) the *Cataloged Galaxies and Quasars Observed in the IRAS Survey* (Lonsdale *et al.* 1985). For the latter, only the galaxies that contribute to at least 10% of the cloud IR flux have been associated. Thus, the well-known nearby galaxies Messier 31, 33, 81, 82, and 101 are listed as associations in Table 1 (the Magellanic Clouds are also associated). A comparison of Table 1 and the catalogs of H II regions by Blitz, Fich, and Stark (1982) and the O star clusters by Humphreys (1978) was also performed by a simple coordinate inspection. The statistics of associations (1, 2, and 3) are discussed in § V.

V. DISCUSSION

a) Association with Known Molecular Clouds

The large molecular clouds like the Ophiuchus, Orion, Perseus, Taurus, and Cepheus clouds (Dame *et al.* 1987; Ungerechts and Thaddeus 1987; Lebrun 1986) do appear preeminently in the map of significant clouds shown in Figure 7. However, the method that we used is not optimized for mapping these clouds, because these clouds have sizes comparable to the cell *C*. Furthermore, the present map even shows some large southern extensions of the Taurus cloud near the Eridanus and Cetus regions not yet mapped in CO (especially cloud 276 in Table 1). Therefore, the masses given in Table 1 for these large clouds are probably underestimated, owing to the size of the cell *C* used in the method of § III.

As molecular clouds enter in our category of IRECs, it is important to compare our catalog (Table 1) with MBM's catalog. Of the 123 entries in the MBM list, 59 (=48%) are associated to an entry in Table 1. This result can be decomposed as follows: (1) for $|b| > 25°$, 27 (=47%) out of 57 MBM clouds are associated with 18 different IRECs; (2) for $20° \leq |b| \leq 25°$, 32 (=48%) out of 66 MBM clouds are associated with eight IRECs. Obviously, several clouds belong to the same IREC and correspond to the same complex as defined by MBM. We have performed the same comparison with locations in the sky which were shown by MBM *not* to contain CO at the level of brightness of 0.1 K (Magnani 1987). Among the 340 points without CO emission, we were able to associate only 51 (=15%) to IRECs. The comparison between the MBM survey and the present analysis is not straightforward

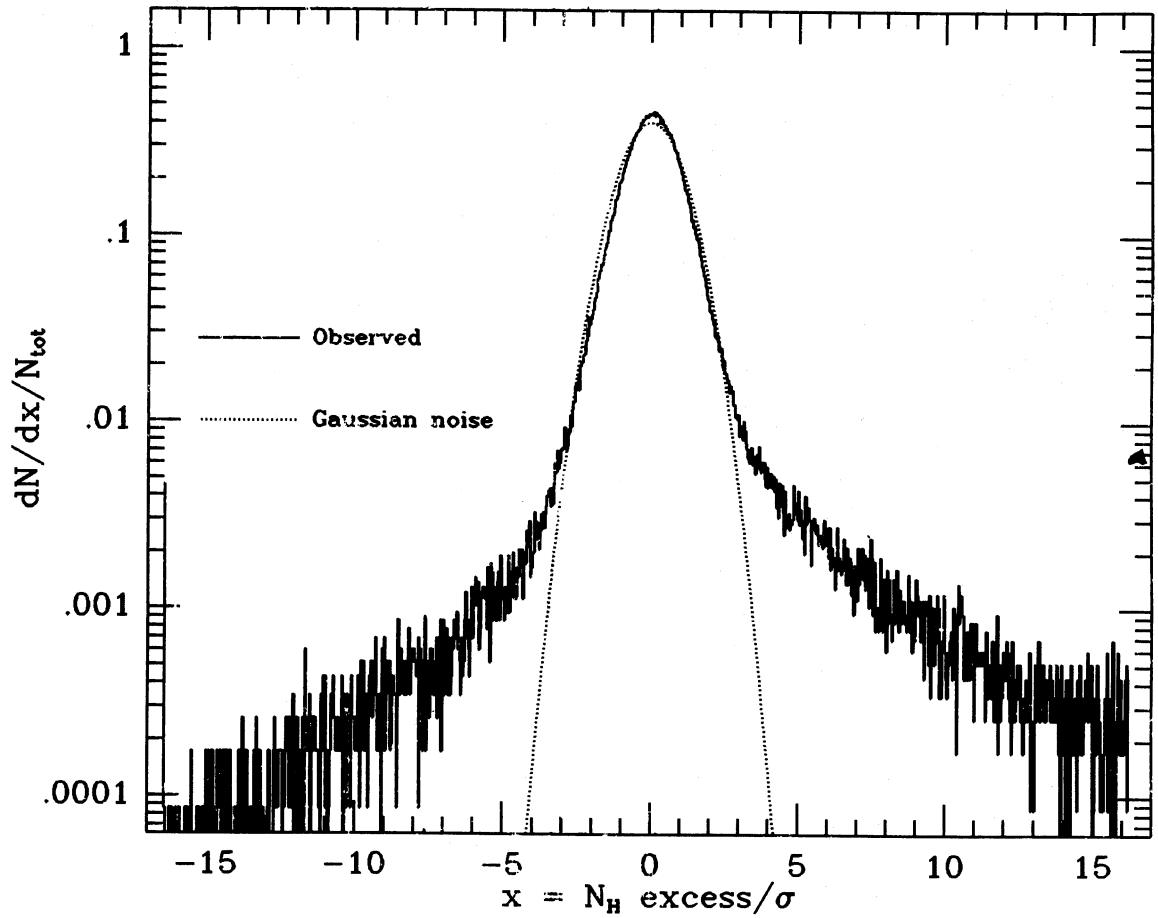

FIG. 8.—Solid line is the distribution of the ratio x of hydrogen excess column density N_H^e to the dispersion measured by σ, for the whole map. Dotted line represents the expectation from Gaussian noise. The wing of positive excesses is more important than the wing of negative excesses. The origin of the wings is unknown. Point sources could contribute to the positive wing.

because of the different resolutions. Indeed, among the molecular clouds mapped by MBM ($|b| \geq 25°$), the clouds missing in Table 1 generally are small (1 or 2 pixels only) and therefore are not always expected to show up as significant clouds. The four exceptions are MBM clouds 26, 53, 54, and 55. The local correlation IR–H I performed close to the complex 53, 54, 55 may have been biased by these large and diffuse clouds and therefore may have washed out these clouds. One assumption of our method, which is that the molecular clouds occupy a small fraction of the sky, may be wrong for this complex, and, indeed, Figure 4 shows a larger σ than usual at the very location of this complex ($L \approx 110°$, $b \approx 40°$). The missing MBM cloud 26 still remains unexplained.

To show in a way independent from the cloud definition that the known molecular clouds preferentially are where there is an IR excess in our map, we have computed (see Fig. 8) the distribution of IR–excess-to-σ ratio x (equal to the equivalent N_H excess–to–σ_H ratio; formulae [3.3] and [3.4]) for the whole sky. The distribution is close to a Gaussian plus two small asymmetric wings. The positive wing is constituted by large IR-excess points, the nature of which is unknown as well as the negative wing. Then, we computed the histogram of the ratios x taken at the nearest pixel of our map to the MBM cloud centers (see Fig. 9). Clearly, the MBM clouds do not follow the Gaussian distribution of the whole map. The reduced χ^2 (with 31 degrees of freedom) is 17.4. On the other hand, if we compute the distribution of x for the CO nondetection points by MBM (Fig. 9 *dashed line*) we find a reduced χ^2 of 1.00, consistent with these points being randomly chosen in the sky.

The associations with KM southern molecular clouds have also been performed. From the 18 KM clouds, only 2 (= 11%) are in Table 1 (cloud No. 427). As previously mentioned, the accuracy of the present map is the southern hemisphere does not seem to be as good as in the northern hemisphere. However, the small size of the KM sample should prevent us against definitive conclusions. For example, the average KM cloud area is only 0.67 deg^2, i.e. only 6 pixels in our map.

b) Other Possible Associations

We looked for association with the ionized medium by studying the Hα survey by Reynolds (1984). No correlation between the parameter x (see above) and the emission measure of 46 lines of sight is noticed. However, we do find associations of 7 (= 28%) out of the 25 lines of sight that are quoted by Reynolds as within 5° of emission nebulosities visible on photographic surveys, but these associations are close (within 15°) to the Galactic plane and therefore are probably contaminated by discrete H II regions. That this is indeed the case can be shown by comparing the catalog of runaway O stars by Bekenstein and Bowers (1974) with our catalog. Twenty-two

(= 40%) out of 55 positions of runaway stars are associated with an IREC. This proportion decreases outside the Galactic plane: only four (= 23%) out of the 17 directions which satisfy $|b_{II}| > 5°$ are associated with a cloud in Table 1. We conclude that some of the low-latitude clouds in our survey are close to H II regions. The comparison of Table 1 and the H II region catalogs by Blitz, Fich, and Stark (1982) and Humphreys (1978) confirms this view.

High-velocity clouds (HVCs), if they had the usual gas-to-dust ratio, would show up in our map, because this H I medium is not in the velocity range sampled by the used H I survey (see § II). We have selected among the H I observations by Hulsbosch (1975) the 60 HVCs with a velocity satisfying $|v| > 100$ km s^{-1} and $|b| > 5°$. We could associate only five of them (= 8%) to clouds in our catalog. These are (in l, b, v coordinates) HVC 107.5+8.3−136 (141), 66+39.5−121 (96), 92+38−149 (113, possible confusion with the Draco Nebula at $v = -21$ km s^{-1}), 90+35−165 (116), and 102+26−102 (No. 129) (numbers in parenthesis refer to the Table 1.) Beside these possible associations—they need some support from observations (they could all be accidental)—most of the HVCs do not appear in Table 1. A previous work by Wakker and Boulanger (1986) had shown the absence of some well-studied HVCs in the *IRAS* survey. Following their analysis, we merely emphasize that the likely explanation is that the HVCs are dust deficient. The Magellanic Stream (Mathewson, Cleary, and Murray 1974) does not clearly appear in the present catalog in agreement with Fong *et al.* (1987): the only possible associations are the HVC301−15+292 (432) (Morras 1982), and MS VI 86.9−42.2 (109) (Mirabel 1982). However, the concentration of clouds at $l_{II} \approx 300°$ and b_{II} between −40° and 0° may be related to the Magellanic Clouds (or more probably to the Chameleon molecular cloud: e.g., cloud 432; see Boulanger *et al.* 1988) but more H I and CO observations, with a wide velocity range, would be needed to address that question.

Finally, only 16 clouds (3%) in Table 1 are firmly associated with extended nearby galaxies or groups of galaxies. Thirty-one other clouds are contaminated by galaxies at a level between 1% and 10%. The remaining 469 clouds are definitely not produced by the known galaxies. Other possible associations of the clouds with extragalactic objects (clusters, unknown galaxies ...) are possible but unlikely to change the above proportions by much.

In summary, H II regions and star-forming regions near the Galactic plane are likely to correspond to some clouds in Table 1, and away from the Galactic plane (by more than ~10°), neither H II regions, HVCs, nor galaxies can account for a large fraction of the clouds.

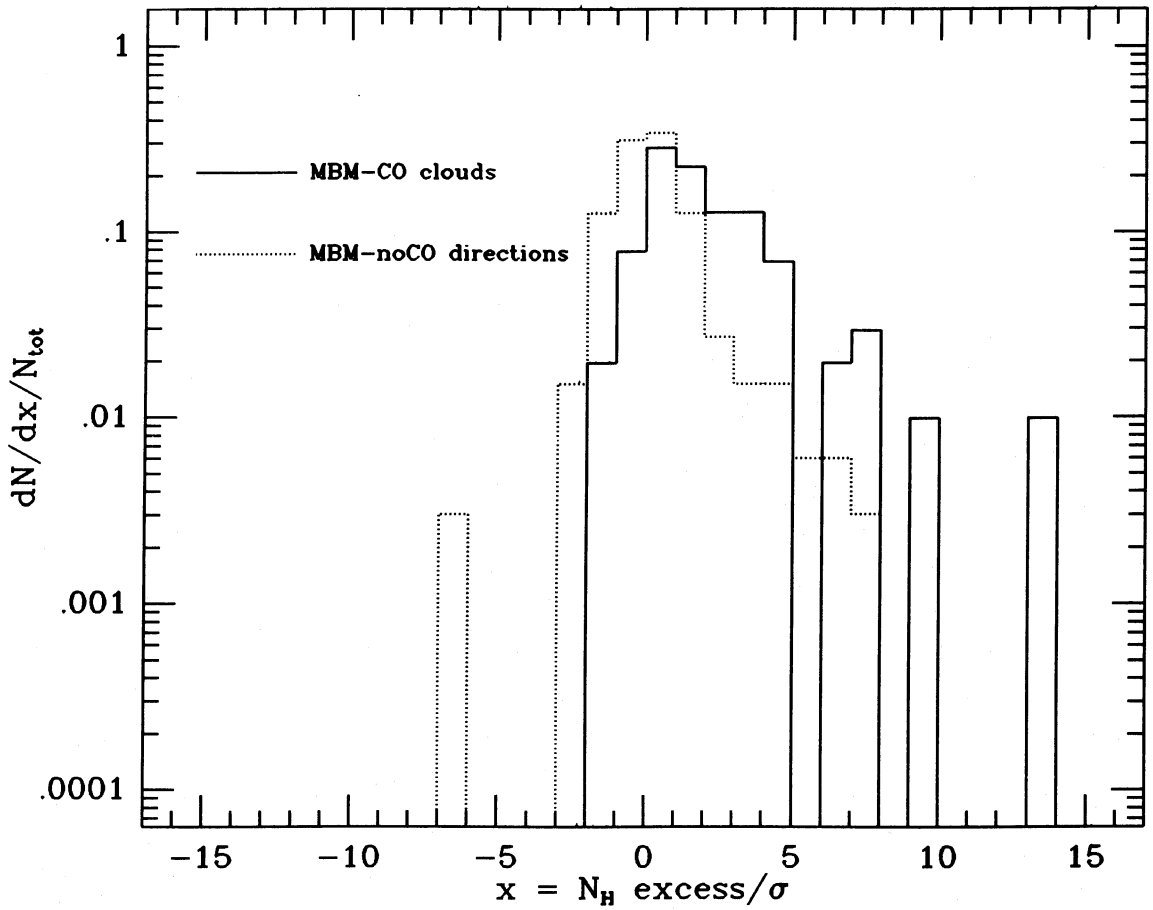

FIG. 9.—The distribution of hydrogen excess (measured by x, *solid line*) in the line of sight of the CO emission peak in the MBM survey is very asymmetric with respect to Fig. 8. On the contrary, the distribution of x (*dotted line*) for the 340 lines of sight where MBM did not detect CO emission show no statistically significant deviations from the general curve of Fig. 8. In other words, locations where CO is detected occur preferentially where x is positive and large.

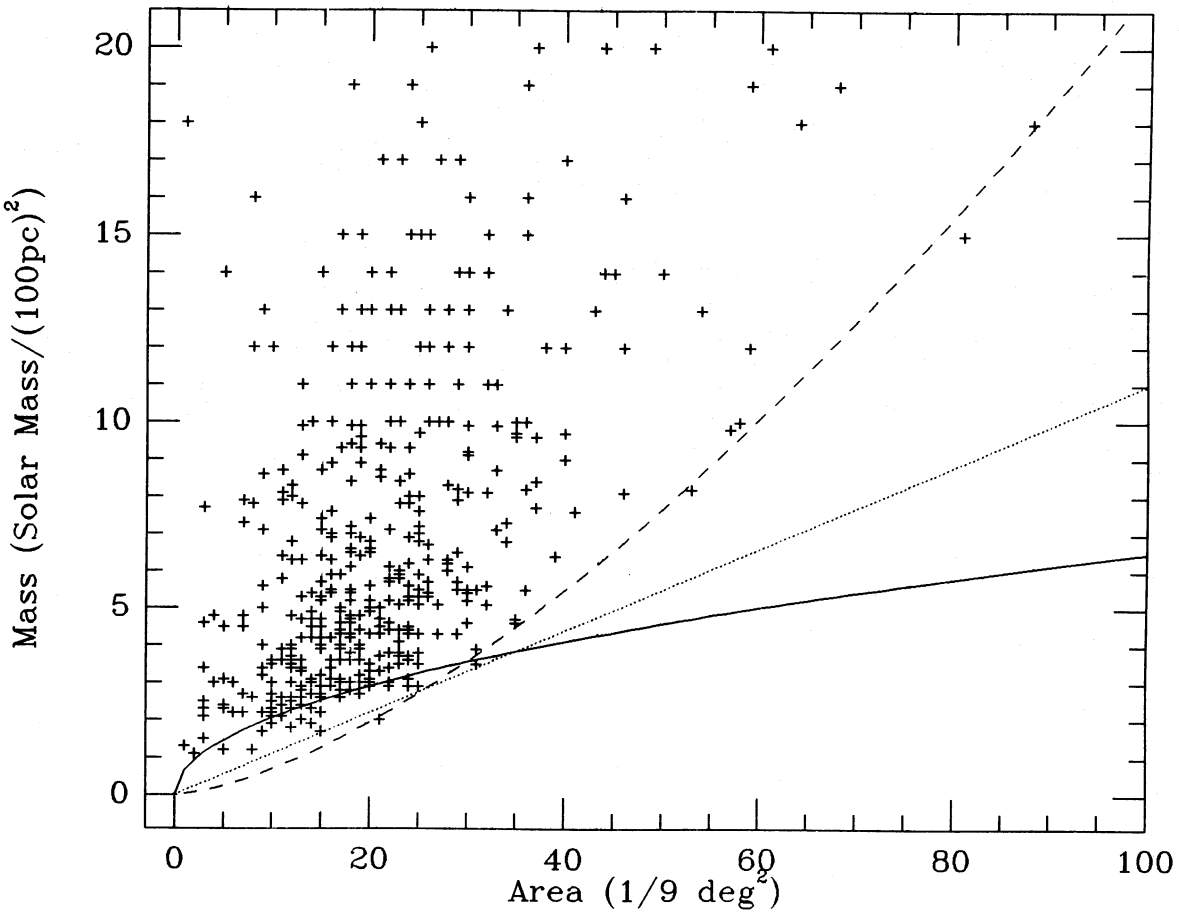

FIG. 10.—Location of the IRECs (*crosses*) of Table 1 in an area-mass diagram. Continuous and dotted lines are the lower limits due the selection criteria, assuming $\sigma = 40 \times 10^{18}$ H cm^{-2}. Dashed curve is an isodensity curve at $n_H = 6$ cm^{-3}, assuming a distance of 100 pc. One can notice the absence of points below this line. The general features of the diagram do not change if we include only the clouds satisfying $|b| \geq 20°$.

c) *Cloud Statistics*

We analyze first the physical parameters that can be deduced from the cloud data in Table 1 and then study the spatial distribution of the clouds. Some of the results shown here are independent of the precise nature of the IRECs.

The relationship between the mass M and the area (measured by n) of the clouds is shown in Figure 10, which is valid under the assumption that the majority of the clouds in Table 1 correspond to local gas clouds. The first constraint (*solid line*) that applies to this diagram is imposed by the value of the significance S_g which must be larger than 4 (using formulae [4.2] and [4.3]):

$$M/D^2 \geq 0.65 n^{1/2} (\sigma/49 \times 10^{18} \text{ H cm}^{-2}) , \qquad (5.1)$$

where the mass M/D^2 is in units of $M_\odot$/(100 pc)^2. The second constraint (*dotted curve*) comes from the definition of 1 σ clouds: inside a cloud,

$$N_H^e \geq \sigma ,$$

which translates with formula (4.3) into

$$M/D^2 \geq 0.11 n (\sigma/40 \times 10^{18} \text{ H cm}^{-2}) . \qquad (5.2)$$

There are some variations of the noise measured by σ (see Fig. 5), that can explain why some clouds are below the two limits (set for $\sigma = 40 \times 10^{18}$ H cm^{-2}) in Figure 10. Nevertheless, there seems to be a deficiency of clouds with large area and small masses (*upper right part of the diagram*). Assuming spherical symmetry for the clouds, one can deduce the average density of the cloud from the following expression:

$$n_H/1 \text{ H cm}^{-3} = 276 M/D^2 (D/100 \text{ pc})^{-1} n^{-3/2} . \qquad (5.3)$$

The lower envelope of the points corresponds to a density of ~ 6 cm^{-3} (assuming $D = 100$ pc) and is shown as the dashed curve in Figure 10. Alternatively, this lower envelope might have been produced by the cloud selection method, however, the size of the cell C seems large (1440 pixels) enough compared with the average area of the clouds. Our method is biased against low-mass extended clouds because they would tend to break into smaller clumps. The most probable value of the density of the clouds is ~ 10 cm^{-3}. This property does not vary if only clouds satisfying $|b| \geq 20°$ are considered. If compared directly with the MBM average value of the density (on average, 280 H cm^{-3}) in high-latitude molecular clouds, the low density found here indicates a low surface filling factor inside each cloud: typically 10% (Magnani (1987) found 30%–70%). On the other hand, VHT have found that the CO to H_2 conversion factor may be lower in diffuse high-latitude clouds by a factor of 5 than what MBM assumed, although VHT study applies to only one region so far. That factor would bring their density to 60 H cm^{-3}, still higher by a factor 6 than what

we found either (1) our method underestimates the mass of the clouds (in our method, the correlation between the IR brightness and the H I data seems to give an overestimated IR-to–H I ratio compared with the cosecant law by an average of 50%) or (2) it extends clouds to lower column density limits than CO observations do.

The median value for the area is $n = 22$ (2.4 deg^2) (20 for $|b| \geq 20°$), which translates for spherical symmetry, into a diameter of 3 pc (MBM give 1.6 pc) at a distance of 100 pc. The median value for the mass is 6.3 solar masses/(100 pc)^2 and 4.8 for clouds with $|b| \geq 20°$; MBM give a median value of 18 for their 23 fully sampled complexes. Boulanger *et al.* (1988) showed that the IR-to-gas ratio is lower inside large molecular clouds than in the diffuse H I medium because of optical depth effects (for $A_V \gtrsim 1$: Boulanger *et al.* 1988; de Vries and Le Poole 1985). It is likely that these effects are less important at high latitudes because the extinction is generally less than 1 mag, and therefore the mass of the IRECs should not be underestimated by this effect. The mass distribution of the clouds (not shown here) closely follows a power law: $N(>M) \approx 1.4 \times 10^3 M^{-0.91 \pm 0.05}$ for masses larger than 4.5 $M_\odot$/(100 pc)^2. Below that limit, the distribution flattens and then decreases for masses less than 3, probably giving an estimate of the completeness limit, and hence the sensitivity of our method.

The IRECs do not tend to be associated with an enhanced surrounding H I medium because, on average, the ratio between the H I column density at the position of the clouds and the expected value from the cosecant law (3.1) at the same galactic latitude is 0.9 (rms = 0.4). However, adding the equivalent excess hydrogen N_H^e to N_{HI}, the total hydrogen column density is 20% larger, on average, than the expected value. On the other hand, MBM have found H I features at the same velocity as the CO emission. In this respect, our analysis is probably coarse because we use only a velocity-integrated H I map.

The distribution of the clouds in latitude is shown in Figure 11. It shows a small asymmetry toward positive latitudes (by 6%). Three hundred fifty-three clouds (68%) among the Table 1 are away from the Galactic plane by more than 20°. The equivalent hydrogen excess N_H^e inside the clouds has been averaged by spreading it over all the longitudes and at constant latitude. For $|b| \geq 30°$, i.e. avoiding all the concentrations corresponding to local giant molecular clouds, this average has a lower envelope roughly following a symmetric cosecant law:

$$\langle N_H^e \rangle = 6 \times 10^{18} \text{ H cm}^{-2}/\sin|b| . \quad (5.4)$$

MBM have found a 30%–70% asymmetry between the northern and southern Galactic hemispheres in the distribution of high-latitude molecular clouds for $|b| > 25°$. Such an asymmetry is not found here, but it may be partly due to the different qualities of the H I data that we used in the southern and northern surveys (see § II*b*) and also our missing the diffuse MBM complex 53–55. From the cosecant law (5.4), which is a lower limit, we derive a surface density of 0.1 $M_\odot$ pc^{-2} for the IR-excess clouds. This density represents a negligible fraction (~2%) of the local density of H I gas (5 $M_\odot$ pc^{-2}). It is also small compared with the estimate of 1.3 for the local density of molecular gas (Dame *et al.* 1987) but compatible with the estimate (made at $|b| \leq 30°$) of 0.2 for small high-latitude molecular clouds (Magnani, Lada, and Blitz 1986).

The fraction of the sky occupied by the clouds slightly decreases with Galactic latitudes; this fraction is 0.059, 0.048, and 0.029 for absolute latitudes larger than 10°, 20°, and 40°, respectively. Magnani, Lada, and Blitz (1986) have found that the surface filling fraction of CO clouds is 0.0045, i.e. much smaller than what we found. Apart from the different resolutions that have been used (which can cause different surface filling factors if the medium is clumpy), this difference could be due to the existence of molecular gas not detectable with CO observations (see § V*d*).

Finally, the logarithmic average value of the maximum of N_H^e inside each cloud is log (2.5 × 10^{20} H cm^{-2}), with a rms dispersion factor of log (2.5), corresponding to ~0.13 mag of visual extinction (using $A_V/N_H = 0.053$ mag/10^{20} H cm^{-2}; Savage and Mathis 1979). On average, the value of $\langle N_H^e \rangle_{\text{cloud}}$ is 1.9 times smaller than the maximum of N_H^e of each cloud.

d) Probable Nature of the IRECs

In view of the above analysis, as H II regions, high-velocity clouds and extragalactic objects do not show up very much in Table 1, the clouds situated outside the Galactic plane are likely to be of two possible natures: (1) molecular clouds, as MBM have described in their CO survey; (2) high dust-to-gas ratio H I clouds or clouds which are more heated than average. A third possibility, the saturation of the 21 cm line, is very unlikely at high Galactic latitudes.

The first possibility, our main motivation, has been partially tested with the MBM sample (see § V*a*). It could be tested further by additional CO observations (for additional precision on the exact centers of the IRECs one could use the *IRAS* Skyflux plates). On the other hand, the nondetection of CO does not totally preclude the existence of molecular clouds. Indeed, for low extinction clouds (A_V less or equal to ~1 mag), a layer of H_2 is predicted to survive where CO molecules would be destroyed by the UV radiation field (see, e.g., Prasad *et al.* 1987; Pérault *et al.* 1985; Mitchell *et al.* 1978). Some observational evidence for that phenomenon is given by Lada and Blitz (1988). Thus, if such an H_2 medium without CO molecules exists, our surface filling factor would be larger than that of MBM, as is observed.

The second possibility has to be tested further. To detect clouds which are more heated than the average, one could use the 60 μm *IRAS* map in order to determine if the 60 to 100 μm ratio is larger than the usual cirrus value in some clouds; however, the heating source(s) should be easy to locate. Indeed, the energy density of the radiation field, at a distance r (which can be taken as the extent of the cloud) from the source(s) (of luminosity L) has to be at least of the order of the ISFR energy density (~0.4 eV cm^{-3}); hence, $L > 600\ L_\odot\ (r/1\text{ pc})^2$. On the other hand, if the ISRF is uniform enough, an important fraction of clouds could simply be locally dustier than the average by ~33% on average, as deduced from the value of $\langle N_H^e \rangle / \langle N_{HI} \rangle$ inside each IREC and averaged over all the clouds (the median is 22%). A less likely possibility, but which is difficult to address without additional observations (see § V*b*), is some concentrations of dusty ionized gas.

e) Weaknesses of the Method

The method is rather straightforward but has the following limitations: (1) the resolution prevents us from seeing small clouds (some small MBM cloudlets are not associated with IRECs in Table 1); (2) the size of the correlation analysis cell C prevents us from seeing very extended clouds with low contrast, whether they exist or not, and distorts the picture of the largest molecular clouds: Orion, Ophiuchius, Taurus; (3) the

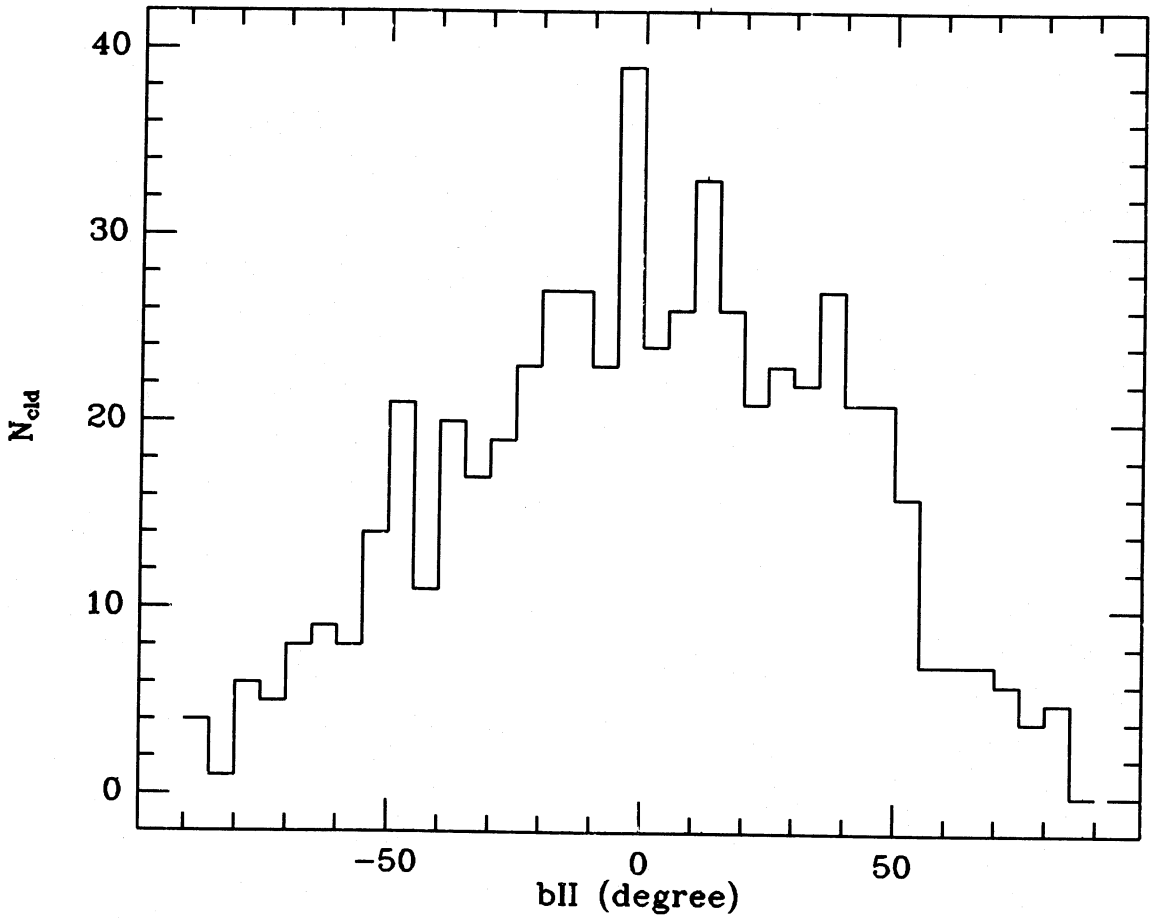

FIG. 11.—Repartition of the number of significant IRECs as a function of the Galactic latitude of their center

stripiness of the initial maps necessarily introduces some noise in the results (10% of the clouds in Table 1 have been visually identified as defects in the H I or *IRAS* maps and are likely to be spurious); (4) the reliability of Table 1 is difficult to assess; the comparison with known molecular clouds (MBM and § V*a*) allows us to see that the corresponding entries in Table 1 are relatively significant ones: the median value of S_g (respectively of the area) for MBM entries is 11 (respectively 64 pixels) compared with 5.2 (respectively 22) for the whole Table 1. Some remedy to these limitations should be found by the analysis of sky flux plates with few arcminute resolution combined with H I and CO observations, as first worked out by Weiland *et al.* (1986) and VHT. A preliminary analysis of the 4′ resolution *IRAS* maps at 100 μm shows that $\sim$80% of the entries in Table 1 correspond to well-identified structures in the IR maps.

f) Infrared-deficient Clouds

Our study was focused on the parts of the sky that show an *excess* of IR emission relative to the H I expectation. However, we did perform the same analysis for the clouds which present, in a significant way, a *deficit* of IR emission relative to the H I expectation. An all-sky list (similar to Table 1) of $\sim$700 significant clouds is available upon request. A preliminary analysis of this list reveals that: (1) only one MBM cloud (No. 3) is associated with the list; (2) 22 (6.5%) clouds out of the 340 directions where CO was not detected by MBM (see § V*a*) are associated with the list (compatible with random associations); (3) the H I column density at the location of the clouds is enhanced by 30% relative to the average cosecant law. A sample comparison of the list with the velocity-longitude H I maps given by Heiles and Habing (1974) shows that some clouds of the list may be produced by some intermediate-velocity H I clouds (IV*c*, $20 < |v| < 60$ km s^{-1}), although the correspondence is far from one-to-one. Indeed, if some IVCs are dust deficient or have an anomalous grain size distribution (probably because of shocks), they are expected to show up in this list of IR-deficient clouds. Table 2 gives some examples of the associations, where each line gives the cloud number in the list, the Galactic coordinates, a rough estimate of the velocity (from Heiles and Habing 1974 maps), the area (in pixel units), and the estimated fraction F_{miss} of missing H I mass to account for the IR deficit.

g) Summary

After having correlated the H I column density with the IR 100 μm brightness (see BP), we have attempted to find regions at high Galactic latitudes where there is significantly more infrared emission than can be accounted for by the H I medium only. Table 1 lists the location and the properties of these regions called infrared-excess clouds IRECs which satisfy $|b_{II}| \geq 5°$. By associating these IRECs with previously known objects, the following percentages of entries in Table 1 were found: (1) MBM or KM high-latitude molecular clouds (5%);

TABLE 2

EXAMPLES OF INFRARED-DEFICIENT CLOUDS ASSOCIATED WITH IVCs

Cloud	l_{II}	b_{II}	v (km s^{-1})	Area (pixels)	F_{miss}
122.....	70°0	53°3	−20	31	0.13
139.....	89.1	−39.0	−50	77	0.13
153.....	94.9	−19.3	−20	38	0.11
160.....	98.4	30.0	−50	19	0.14
169.....	101.7	68.0	−30	17	0.22
182.....	107.7	28.3	−30	58	0.15
235.....	135.0	53.7	−40	24	0.22
244.....	142.1	−68.3	−50	26	0.12
264.....	155.6	−68.3	−50	59	0.22
403.....	229.8	75.7	−40	18	0.14
458.....	248.0	69.3	−30	15	0.15
476.....	254.1	74.3	−30	59	0.17
489.....	261.5	30.3	+50	21	0.13
516.....	272.6	54.3	−30	15	0.45
559.....	292.2	38.3	±50	16	0.08
570.....	297.7	38.3	±50	45	0.10

(2) H II regions (3%); (3) external galaxies (3%). A fraction of ~10% of the entries can be due to various problems in the initial data or in the method used here. The nature of the remaining 79% of Table 1 is unknown at present. However, it is very unlikely that a significant fraction of the remaining IRECs is made of unknown H II regions, galaxies, or high-velocity clouds. It is more likely that a large fraction of the IRECs in Table 1 merely corresponds to high-latitude molecular cirrus clouds. In this case, these clouds, not including the surrounding H I medium, would have, on average, a projected area of 2.4 deg^2, a diameter of 3 pc, a mass of 8 solar masses, and a density of 10 cm^{-3} (if at a distance of 100 pc). These clouds cover a small fraction (less than 5% for $|b| \geq 20°$) of the high-latitude sky and have a mass surface density of $\sim 0.1\ M_\odot$ pc^{-2}. A test of the molecular nature of these IRECs, now under way, can be performed with the observations of the radio CO transitions, although theoretical models predict that some clouds may contain some molecular hydrogen without CO molecules.

We thank M. G. Hauser, D. T. Leisawitz, L. Magnani, and F. Verter for many discussions and helpful suggestions. This work was done while one of us (F. X. D.) held a National Research Council Research Associateship at the Infrared Astrophysics Branch, Laboratory for Astronomy and Solar Physics at NASA Goddard Space Flight Center.

APPENDIX

SUMMARY OF THE CORRELATION ANALYSIS METHOD

From the H I and IR data described in § II, perform the following steps for each cell C of the sky:

1. Remove the global cosecant laws for both the H I and IR data, given by formulae (3.1); then remove points brighter than 8 MJy sr^{-1}.
2. Compute the least-square fit values of the slope S_{4h}, the intercept I_{4h}, and the rms dispersion σ among all the pixels in the cell C.
3. Discard the points that are more than $\pm 5\ \sigma$ away from the fitted line.
4. Compute the H I–related background G_h (function of b in the northern hemisphere and of δ in the southern one) given by formula (3.6), corresponding to H I stripes, and subtract it from the H I data.
5. Repeat steps 2 and 3.
6. Compute the IR–related background (*IRAS* stripes taken at constant ecliptic longitude) and subtract it from the IR data.
7. Repeat steps 2 and 3.
8. Finally, compute the residuals from the last fitted line with a formula similar to (3.4) and (3.7), for *all* the pixels inside the small cell C' (which is included in the cell C).

REFERENCES

Beichman, C. A., Neugebauer, H. J., Habing, H. J., Clegg, P. E., and Chester, T. J., eds. 1985, *IRAS Explanatory Supplement* (Washington, DC: US Government Printing Office).
Bekenstein, J. D., and Bowers, R. L. 1974, *Ap. J.*, **190**, 653.
Blitz, L., Fich, M., and Stark, A. A. 1982, *Ap. J. Suppl.*, **49**, 183.
Blitz, L., Magnani, L., and Mundy, L. 1984, *Ap. J. (Letters)*, **282**, L9.
Boulanger, F., Baud, B., and van Albada, G. D. 1985, *Astr. Ap.*, **144**, L9.
Boulanger, F., Cohen, R. S., Gaida, M., Grenier, I., Koprucu, M., Maddalena, R. J., Thaddeus, P., and Ungerechts, H. 1988, preprint.
Boulanger, F., and Pérault, M. 1988, *Ap. J.*, **330**, 964 (BP).
Burstein, D., and Heiles, C. 1978, *Ap. J.*, **225**, 40.
Colomb, F. R., Pöppel, W. G. L., and Heiles, C. 1980, *Astr. Ap. Suppl.*, **40**, 47.
Dame, T. M., *et al.* 1987, *Ap. J.*, **322**, 706.
de Vries, C. P., and Le Poole, R. S. 1985, *Astr. Ap.*, **145**, L7.
de Vries, H. W., Heithausen, A., and Thaddeus, P. 1987, *Ap. J.*, **319**, 723 (VHT).
Fong, R., Jones, L. R., Shanks, T., Stevenson, P. R. F., Strong, A. W., Dawe, J. A., and Murray, J. D. 1987, *M.N.R.A.S.*, **224**, 1059.
Heiles, C., and Habing, H. J. 1974, *Astr. Ap. Suppl.*, **14**, 1.
Heiles, C., Stark, A. A., and Kulkarni, S. 1981, *Ap. J. (Letters)*, **247**, L73.
Henderson, A. P., Jackson, P. D., and Kerr, F. J. 1982, *Ap. J.*, **263**, 116.
Hulsbosh, A. N. M. 1975, *Astr. Ap.*, **40**, 1.
Humphreys, R. M. 1978, *Ap. J. Suppl.*, **38**, 309.
Kerr, F. J. 1968, in *Nebulae and Interstellar Matter*, ed. B. M. Middlehurst and L. H. Aller (Chicago: University of Chicago Press), p. 575.
Keto, E. R., and Myers, P. C. 1986, *Ap. J.*, **304**, 466 (KM).
Lada, E. A., and Blitz, L. 1988, *Ap. J. (Letters)*, **326**, L69.
Lebrun, F. 1986, *Ap. J.*, **306**, 16.
Lockman, F. J., Jahoda, K., and McCammon, D. 1986, *Ap. J.*, **302**, 432.
Lonsdale, C. J., Helon, G., Good, J. G., and Rice, W., eds. 1985, *Catalogued Galaxies and Quasars Observed in the IRAS Survey*, preliminary version.
Low, F. J., *et al.* 1984, *Ap. J. (Letters)*, **278**, L19.
Magnani, L. 1987, Ph.D. thesis, University of Maryland.
Magnani, L., and Blitz, L. 1985, in *Proc. ESO Conf. and Workshop No. 22, ESO-IRAM-Onsala (Sub)millimeter Astronomy*, ed. P. A. Shaver and K. Kjär (Munich: ESO), p. 257.
Magnani, L., Blitz, L., and Mundy, L. 1985, *Ap. J.*, **295**, 402 (MBM).
Magnani, L., and de Vries, C. P. 1986, *Astr. Ap.*, **168**, 271.
Magnani, L., Lada, E., and Blitz, L. 1986, *Ap. J.*, **301**, 395.
Mathewson, D. S., Cleary, M. N., and Murray, J. D. 1974, *Ap. J.*, **190**, 291.
Mirabel, I. F. 1982, *Ap. J.*, **256**, 112.
Mitchell, G. F., Ginsburg, J. L., and Kuntz, P. J. 1978, *Ap. J. Suppl.*, **38**, 39.
Morras, R. 1982, *Astr. Ap.*, **115**, 249.
Pérault, M., Boulanger, F., Falgarone, E., and Puget, J. L. 1988, *Ap. J.*, submitted.
Pérault, M., Falgarone, E., and Puget, J. L. 1985, *Astr. Ap.*, **152**, 371.
Prasad, S. S., Tarafdar, S. P., Villere, K. R., and Huntress, W. T. 1987, in *Interstellar Processes*, ed. D. J. Hollenbach and H. A. Thronson (Dordrecht: Reidel), p. 631.

Reynolds, R. J. 1984, *Ap. J.*, **282**, 191.
Savage, B. D., and Mathis, J. S. 1979, *Ann. Rev. Astr. Ap.*, **17**, 73.
Sodroski, T. J., Dwek, E., Hauser, M. G., and Kerr, F. J. 1987, *Ap. J.*, **322**, 101.
Ungerechts, H., and Thaddeus, P. 1987, *Ap. J. Suppl.*, **63**, 645.
Wakker, B. P., and Boulanger, F. 1986, *Astr. Ap.*, **170**, 84.
Weaver, H., and Williams, D. R. W. 1973, *Astr. Ap. Suppl.*, **8**, 1.
Weiland, J. L., Blitz, L., Dwek, E., Hauser, M. G., Magnani, L., and Rickard, L. J. 1986, *Ap. J. (Letters)*, **306**, L101.

D. BAZELL: Applied Research Corporation, 8201 Corporate Drive, Landover MD 20785

F. BOULANGER: Infrared Processing and Analysis Center, California Institute of Technology 100-22, Pasadena, CA 91125

F. X. DÉSERT: NASA Code 685, Goddard Space Flight Center, Greenbelt, MD 20771